Posted on 30 Nov 2022 — The copyright holder is the author/funder. All rights reserved. No reuse without permission. — https://doi.org/10.1002/essoar.10505736/v1 — This a preprint and has not been peer reviewed. Data may be preliminary.

Complicated lithospheric structure beneath the contiguous US revealed by teleseismic S reflections

Tianze Liu[1,1] and Peter M. Shearer[2,2]

[1]University of California, San Diego
[2]U.C. San Diego

November 30, 2022

Abstract

Lithospheric discontinuities, including the lithosphere-asthenosphere boundary (LAB) and the enigmatic mid-lithospheric discontinuities (MLDs), hold important clues about the structure and evolution of tectonic plates. However, P- and S-receiver-function techniques (PRF and SRF), two traditional techniques to image Earth's deep discontinuities, have some shortcomings in imaging lithosphere discontinuities. Here, we propose a new method using reflections generated by teleseismic S waves (hereafter S reflections) to image lithospheric discontinuities, which is less affected by multiple phases than PRFs and has better depth resolution than SRFs. We apply this method to data collected by the Transportable Array and other regional seismic networks and obtain new high-resolution images of the lithosphere below the contiguous US. Beneath the tectonically active Western US, we observe a negative polarity reflector (NPR) in the depth range of 60–110 km, with greatly varying amplitude and depth, which correlates with active tectonic processes. We interpret this feature as the lithosphere-asthenosphere boundary below the Western US. Beneath the tectonically stable Central and Eastern US, we observe two NPRs in the depth ranges of 60–100 km and 100–150 km, whose amplitude and depth also vary significantly, and which appear to correlate with past tectonic processes. We interpret these features as mid-lithospheric discontinuities below the Central and Eastern US. Our results show reasonable agreement with results from PRFs, which have similar depth resolution, suggesting the possibility of joint inversion of S reflections and PRFs to constrain the properties of lithospheric discontinuities.

Complicated lithospheric structure beneath the contiguous US revealed by teleseismic S reflections

Tianze Liu[1], **Peter M. Shearer**[1]

[1]Institute of Geophysics and Planetary Physics, Scripps Institution of Oceanography, UC San Diego

Key Points:

- The LAB in the Western US is 60–110 km deep and correlates well with active tectonic processes.
- Two MLDs exist in the Central and Eastern US in the depth range 60–100 km and 100–150 km, which correlate with past tectonic processes.
- Our results agree well with the results of P receiver functions in many areas.

Corresponding author: Tianze Liu, tianzeliu@ucsd.edu

Abstract

Lithospheric discontinuities, including the lithosphere-asthenosphere boundary (LAB) and the enigmatic mid-lithospheric discontinuities (MLDs), hold important clues about the structure and evolution of tectonic plates. However, P- and S-receiver-function techniques (PRF and SRF), two traditional techniques to image Earth's deep discontinuities, have some shortcomings in imaging lithosphere discontinuities. Here, we propose a new method using reflections generated by teleseismic S waves (hereafter S reflections) to image lithospheric discontinuities, which is less affected by multiple phases than PRFs and has better depth resolution than SRFs. We apply this method to data collected by the Transportable Array and other regional seismic networks and obtain new high-resolution images of the lithosphere below the contiguous US. Beneath the tectonically active Western US, we observe a negative polarity reflector (NPR) in the depth range of 60–110 km, with greatly varying amplitude and depth, which correlates with active tectonic processes. We interpret this feature as the lithosphere-asthenosphere boundary below the Western US. Beneath the tectonically stable Central and Eastern US, we observe two NPRs in the depth ranges of 60–100 km and 100–150 km, whose amplitude and depth also vary significantly, and which appear to correlate with past tectonic processes. We interpret these features as mid-lithospheric discontinuities below the Central and Eastern US. Our results show reasonable agreement with results from PRFs, which have similar depth resolution, suggesting the possibility of joint inversion of S reflections and PRFs to constrain the properties of lithospheric discontinuities.

1 Introduction

The structure of the lithosphere-asthenosphere system is fundamental to understanding plate tectonics and Earth's evolution.Continental lithosphere, which is far more complicated than its oceanic counterpart due to the imprints left by numerous geologic processes during its long life, has drawn great attention from the seismological community (e.g., Rychert et al. (2005), Rychert and Shearer (2009), Levander and Miller (2012), S. M. Hansen et al. (2015), Hopper and Fischer (2018), L. Liu and Gao (2018), and Kind et al. (2020)). However, despite decades of efforts in seismically imaging the continental lithosphere, several fundamental questions regarding seismic discontinuities in the lithosphere-asthenosphere system remain open: What is the depth to the lithosphere-asthenosphere boundary (LAB)? Is the LAB a sharp boundary or a transition zone that spans many tens of kilometers? Does the lithosphere have internal layering, which has been invoked to explain the observations of mid-lithospheric discontinuities (MLDs; e.g., Savage and Silver (2008), Ford et al. (2010)), and how do the aforementioned characteristics of lithospheric discontinuities vary across different geologic provinces? These questions motivate further seismic studies to better resolve lithospheric discontinuities beneath continents.

Traditionally, P and S receiver-functions (SRF and PRF) are widely used for imaging lithospheric discontinuities (e.g.,Rychert and Shearer (2009), Levander and Miller (2012), S. M. Hansen et al. (2015), and Hopper and Fischer (2018)). However, both PRF and SRF have some limitations that hamper their utility in imaging lithospheric interfaces. For PRF, multiple reflected phases generated at the Moho and intra-crustal interfaces arrive in the same time window as P-to-S conversions from lithospheric discontinuities and cause strong interference (Fig. 1d). For SRF, although the S-to-P conversions arrive before direct S and thus do not suffer interference of crustal multiple phases, the significantly lower frequency band of teleseismic S waves than P waves causes SRFs to have lower depth resolution than PRFs (Fig. 1e), which prevents imaging detailed structures within the lithosphere. In addition, the very long periods and small temporal separations between conversions at the Moho and shallow lithospheric discontinuities cause potential interference between the side lobes of the Moho conversions and the lithospheric discontinuity conversions of interest (Kind et al. (2020); Fig. 1e), further complicating the interpretation of SRF images.

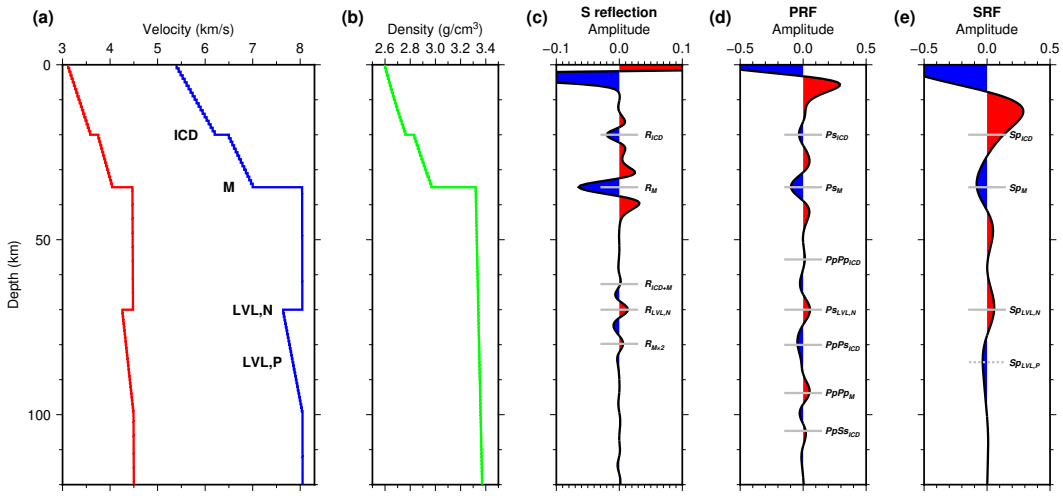

Figure 1. Synthetic examples of imaging lithospheric discontinuities with S reflections, P receiver functions (PRF), and S receiver functions (SRF). The S-reflection and SRF waveforms are computed using a Ricker source wavelet with a median frequency of 0.2 Hz, and the PRF waveform is computed using a Ricker source wavelet with a median frequency of 0.5 Hz (a) 1D V_p (blue) and V_s (red) models used for computing synthetic waveforms. ICD: intra-crustal discontinuity. M: Moho. LVL,N: Negative velocity gradient zone associated with the low-velocity layer (LVL). LVL,P: Positive velocity gradient zone associated with the LVL. (b) 1D density model used for computing synthetic waveforms. (c) S-reflection waveforms computed with the models in (a) and (b) and mapped to depth domain using the same velocity model. (d) P receiver-function waveforms (without deconvolution) computed with the models in (a) and (b) and mapped to depth domain using the same velocity model. (c) S receiver-function waveforms (without deconvolution) computed with the models in (a) and (b) and mapped to depth domain using the same velocity model. Note that the image from teleseismic S reflections has less interference from crustal multiples than the one from PRFs and has higher depth resolution than the one from SRFs.

Recently, Shearer and Buehler (2019) proposed using topside reverberations generated by transverse-component teleseismic S waves to image upper-mantle discontinuities (Fig. 2). This method has two major advantages over PRF and SRF in imaging lithospheric discontinuities. First, multiple reflection phases are much weaker than single reflections because the former undergo additional reflections (Fig. 1c), in contrast to multiples in PRF, which typically have comparable amplitude to the conversions (Fig. 1d). Thus, images of lithospheric discontinuities derived with S reflections suffer less interference from crustal multiples than the ones derived with PRFs (Figs. 1c, d). Second, although both S reflections and SRF utilize long-period teleseismic S waves, the temporal separation between different arrivals is much larger on S reflections than on SRFs because the relative arrival time of the S reflection is the two-way S travel time between the interface and the free surface, whereas the relative arrival time of a conversion on SRF is the difference between the one-way S and P travel times from the interface to the free surface. Thus, for a given interface, the S reflection is separated in time from direct S by a factor of about five compared to the equivalent SRF converted phase, which means that S-reflection imaging provides much better depth resolution than SRF imaging for data over a similar frequency band (Figs. 1c, e). However, a shortcoming of S-reflection imaging is that, for a global discontinuity, an event above it generates reverberations at both the source side and receiver side (gray rays in Fig. 2), which arrive at approximately the same time and complicate the interpretation of the image. To address this issue, Shearer and Buehler (2019), which used only events shallower than 50 km, applied an inversion technique to separate global source-side structure from receiver-side structure beneath the Transportable Array (TA). Despite the success of this approach for imaging the 410- and 660-km discontinuities, it cannot completely eliminate some inherent non-uniqueness between source- and receiver-side structure in the inversion, which could cause artifacts in the resulting images.

To reduce contamination from source-side structure, here we analyze S reflections of earthquakes deeper than 150 km to image receiver-side structures shallower than the event focal depths. In this case, direct topside reflections from a layer above 150 km occur only at the receiver side (blue rays in Fig. 2), which eliminates the need for the inversion procedure in Shearer and Buehler (2019). Note that underside reflections from interfaces shallower than the event focal depths may be generated near the source, but these arrivals will not stack coherently over varying source depths. We apply this method to data collected by both TA and other regional seismic networks in the contiguous US and create high-resolution images of lithospheric discontinuities below the Moho in the study region. We find that our images agree reasonably well with PRF results in regions with good data coverage and that many prominent features in our images can be related to the the tectonic evolution of the North America continent.

2 Data and methods

We obtained three-component waveform data for events with magnitude > 5.5, focal depth > 150 km, and epicentral distance between 30° and 120° recorded at TA and all major regional seismic networks in the contiguous US (see Fig. 3 for a station map and Acknowledgement for a list of the seismic networks included). Because the vast majority of deep-focus events are hosted in subduction zones, the back azimuths of our records are limited to a few narrow corridors that contain major subduction zones (Fig. 3a). We use a 150-km minimum event depth for two reasons. First, this guarantees that topside reflections for discontinuities between the surface and 150 km are only generated near the receiver, the depth range that we focus on in this study. Second, this assures that depth phases (sS), which are much stronger than internal discontinuity reflections, arrive outside the time window for reflections from interfaces shallower than 150 km (Fig. 4a). We then lowpass-filter the traces to below 0.1 Hz, downsample them to 1 Hz, rotate the horizontal components to radial and transverse components, and align and nor-

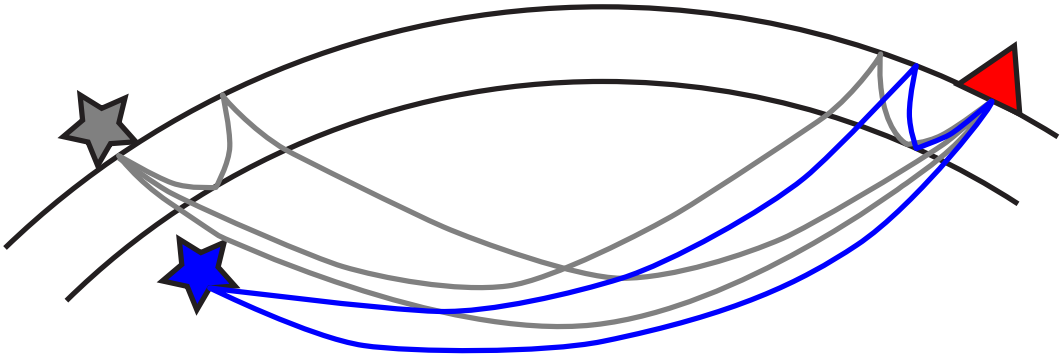

Figure 2. Ray paths of teleseismic S reflections. Note that an event shallower than the discontinuity (gray star) generates both source-side and the receiver-side topside reflections, whereas an event deeper than the discontinuity (blue star) generates only a receiver-side reflection.

malize the transverse components to the maximum amplitude of direct S (Shearer, 1991). We note that although teleseismic S waves should contain some energy up to 0.5 Hz, a corner frequency commonly used by SRF studies (e.g., L. Liu and Gao (2018)), we choose a corner frequency of 0.1 Hz to improve the coherence of our images and concentrate on resolving only large-scale structure. Future S-reflection studies could use higher-frequency data to study regional fine-scale structure of the lithosphere, especially when data from dense local temporary networks is used. Although our stacked S-wave pulse widths are about two times broader than those seen in typical SRF studies, we nonetheless obtain better depth resolution because the temporal separation between topside S reflections is about five times greater than the separation of equivalent conversions in SRFs.

To assure data quality, we define a ± 25 s window around the direct S arrival as the source window and retain only the traces that satisfy the following three criteria: First, the ratio between the mean absolute amplitude (MAA) in the source window and the noise window, defined as the 25 s before the source window, is > 5, which excludes traces with high noise levels. Second, the ratio between the MAA of the source window and the coda window, defined as the 25 s after the source window, is > 1, which excludes traces with abnormally strong coda. Third, the ratio between the maximum amplitude and the MAA in the source window is > 3, which retains only the traces with impulsive source-time functions and thus increases the depth resolution of our images. To further verify our data quality, we plot a record section with the 50,904 traces that passed our selection criteria (Fig. 4a). The record section shows clear direct S and *ScS*, which closely resemble these two phases in Figure 1 in Shearer and Buehler (2019).

We note that our stacking method, both for the record sections discussed here and later when we group data in bins of predicted reflection points, does not involve deconvolution. Rather, we align the traces on the maximum absolute value of the direct S reference phase, flipping the polarity as needed, and normalize the reference peak to unit amplitude. Because these are velocity records, there will typically be a large negative sidelobe either before or after the peak on each trace, so the resulting data stack will have a central peak, with negative sidelobes on each side (Fig. S1). As shown in Fig. S1, the sidelobe amplitudes rarely exceed 0.5 of the central peak, which could be used as a first-order criterion to distinguish negative-polarity reflectors immediately below the Moho from Moho sidelobes (see Section 3.3). Although in principle, these sidelobes might be reduced by using deconvolution or by first correcting the records to displacement, we have found that in practice these approaches can introduce instabilities that complicate interpretation of the results. In contrast, the simple alignment stacking method, when ap-

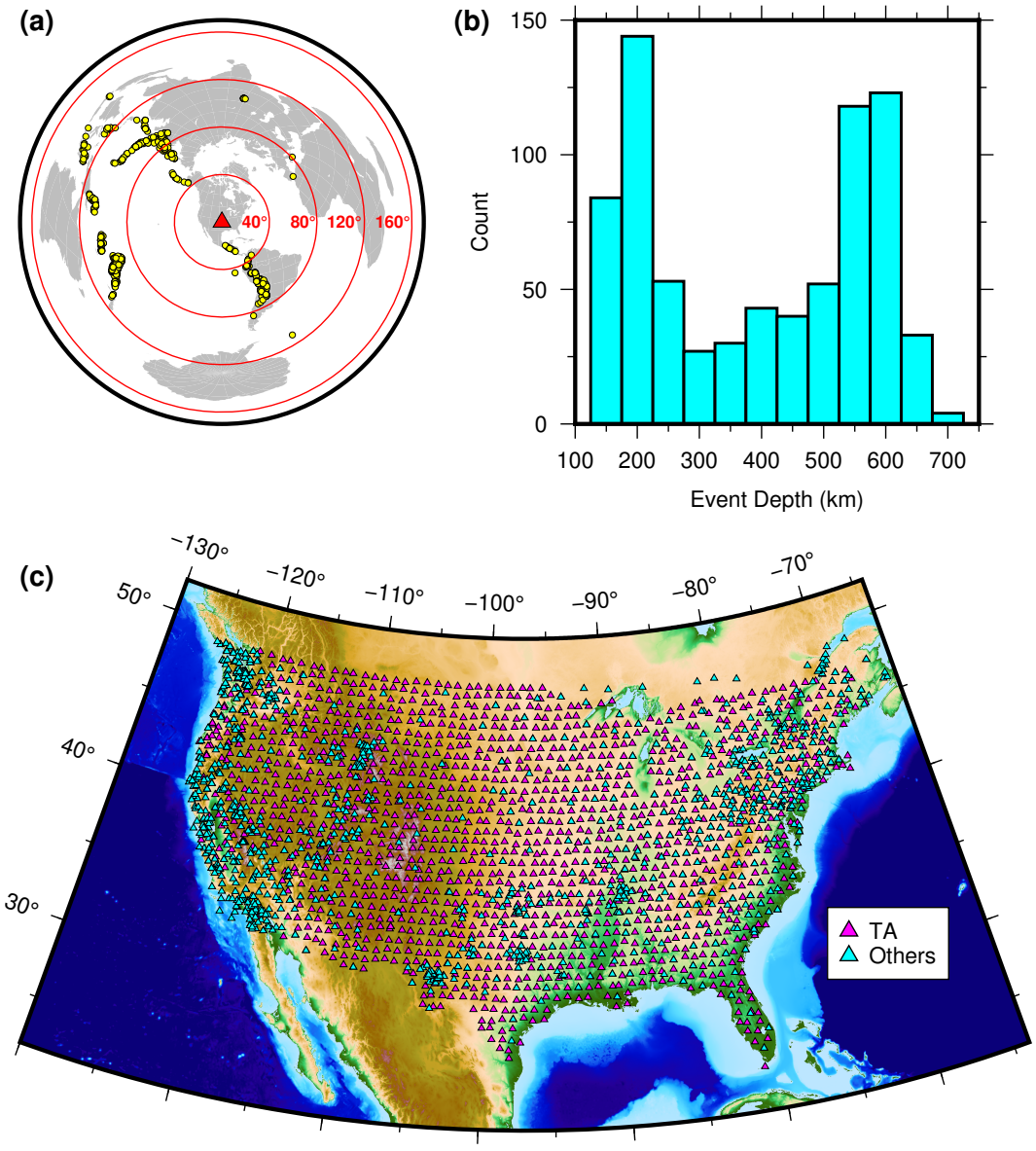

Figure 3. Station and event distribution. (a) Deep events ($\geq$ 150 km) used in our analysis. Concentric circles have radii of 40°, 80°, 120°, and 160°. (b) Depth distribution of the deep events used in our analysis. (c) Stations used in our analysis. Magenta and cyan triangles: The Transportable Array (TA) stations and other regional seismic networks, respectively.

plied to a large number of traces, usually produces a fairly repeatable effective source-time function, which facilitates interpretation and modeling.

Because we use events deeper than 150 km, the part of Figure 4 below the predicted arrival time of *sS* for 150-km focal depth (shown as the gray curve) is dominated by *sS* arrivals and thus does not show clear *Ss410s* and *Ss660s* phases as in Figure 1 of Shearer and Buehler (2019) (which lacked depth-phase interference at those depths owing to the use of shallow events only). The gray curve also marks the arrival time of receiver-side topside S reflections at 150 km because the S reflection at a particular depth arrives at approximately the same time as *sS* from an event at that depth. To further reduce the interference of *ScS* and *sS*, we compute their travel times using the IASP91 model (Kennett & Engdahl, 1991) and mute their amplitude using a Hanning taper around their predicted arrival times. The resulting record section shows clearer *Ss410s* and *Ss660s* phases, especially beyond 95°, indicating successful removal of *sS* interference (Fig. 4b). On the record sections with *ScS* and *sS* muted, we observe a broad band of negative amplitudes in the time window corresponding to reflections between 50 and 150 km depth, implying the presence of negative-polarity reflectors (NPRs) in this depth range. In the rest of this paper, we will always refer to arrivals on S-reflection, PRF, and SRF images that correspond to negative velocity gradients as "negative arrivals" and color them red, while referring to arrivals that correspond to positive velocity gradients (e.g., the Moho) as "positive arrivals" and color them blue. The polarities of the PRF and SRF images are reversed if necessary to make them consistent with our color convention.

Next, we construct common-reflection-point (CRP) images by tracing all the topside S-reflected rays using the IASP91 model (Kennett & Engdahl, 1991) and stacking the amplitudes corresponding to reflection points at each depth into 2°×2° square cells with 1° overlaps in both W-E and S-N directions. The number of rays stacked for each bin (the fold) varies widely (Fig. 5g), mostly due to the uneven distribution of seismic stations (Fig. 3c), with high stacking fold n along the west coast and the Intermountain West Seismic Zone ($n > 600$; Fig. 5g) and low n in most of the Midwest ($n < 100$; Fig. 5g). The profiles generally show positive arrivals at less than 50 km depth, mostly due to the Moho, and negative arrivals between 50 and 150 km depth, likely due to negative-polarity reflectors (NPRs) in the mantle. Before discussing the features seen on our S-reflection profiles in detail, we will first present some general comparisons to receiver function results.

3 Results

3.1 General comparison between S-reflection, SRF, and PRF profiles

Most previous studies of lithospheric discontinuities beneath the contiguous US were derived with SRF (e.g. Hopper and Fischer (2018) and L. Liu and Gao (2018)). Here we will compare our S-reflection images with the SRF results of Hopper and Fischer (2018), which has similar coverage across the US. To compare our images with PRF, we acquired PRFs of the same seismic networks as our study from the IRIS DMC EarthScope Automated Receiver Survey (EARS) (Crotwell & Owens, 2005). We trace the PRF rays with the IASP91 model (Kennett & Engdahl, 1991) and stack the amplitudes at the conversion points into the same grid cells used for our S-reflection CRP images, which gives a PRF common-conversion-point (CCP) image. We extract four W-E profiles A1–A4 and two S-N profiles B1 and B2 (see Fig. 5g for the locations of the profiles) from our S-reflection and PRF image volumes, as well as the SRF image volume of Hopper and Fischer (2018). Fig. 6 shows the comparison between our S-reflection image, the SRF image from Hopper and Fischer (2018), and our PRF image for our W-E Profile A2. Figures S2 and S3 show additional profile comparisons between our results and SRF images from Hopper and Fischer (2018). We flip the polarity of the SRF images so they have the same color convention as the other two images (blue and red indicate impedance/velocity increases and

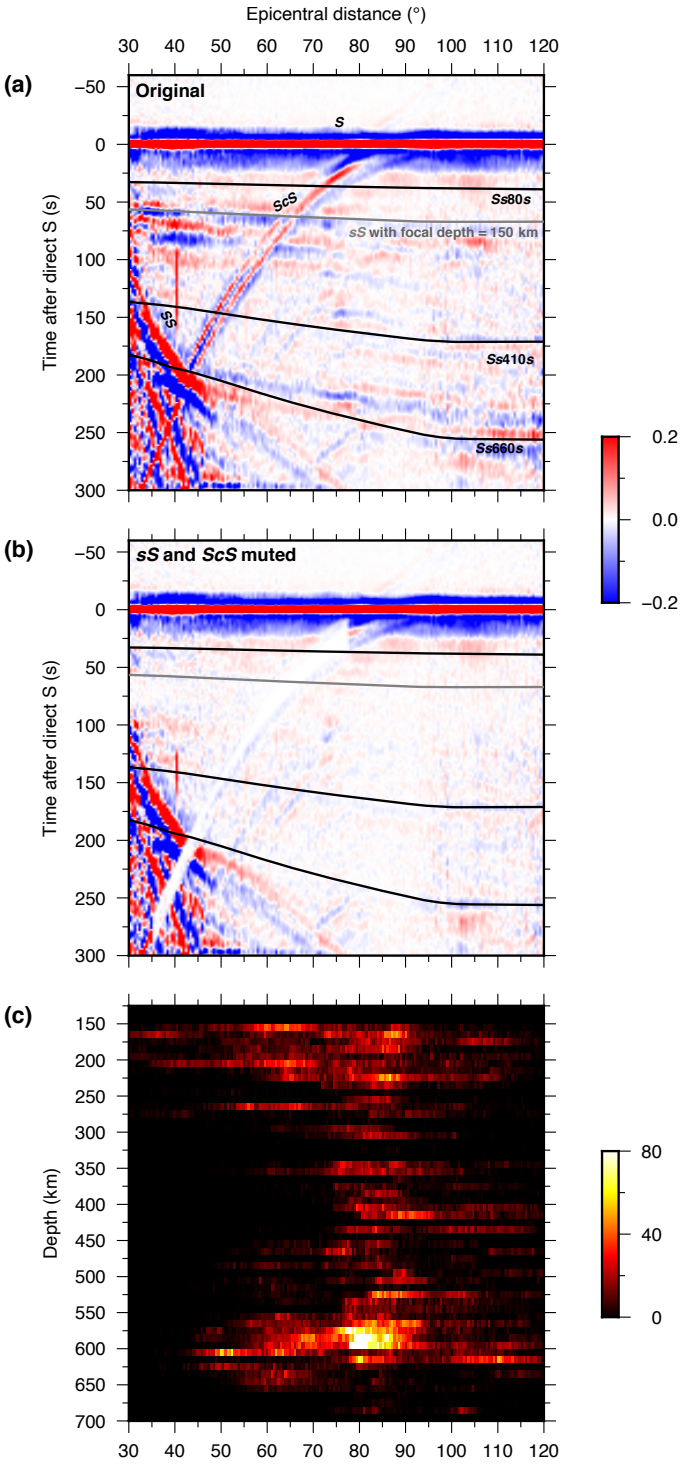

Figure 4. (a) Record section of traces included in our analysis. Note the strong depth phases that overprint reflections deeper than 150 km. The black and gray curves mark the predicted arrival times for reflections at 80, 410, 660 km depth, and *sS* for a focal depth of 150 km, respectively. Also note the interference of *ScS*. (b) The same as (a) but with *sS* and *ScS* muted using their predicted arrival times. Note that the 410 and 660 reflections start to emerge after the interfering *sS* phases are muted. (b) Distribution of event depth and distance.

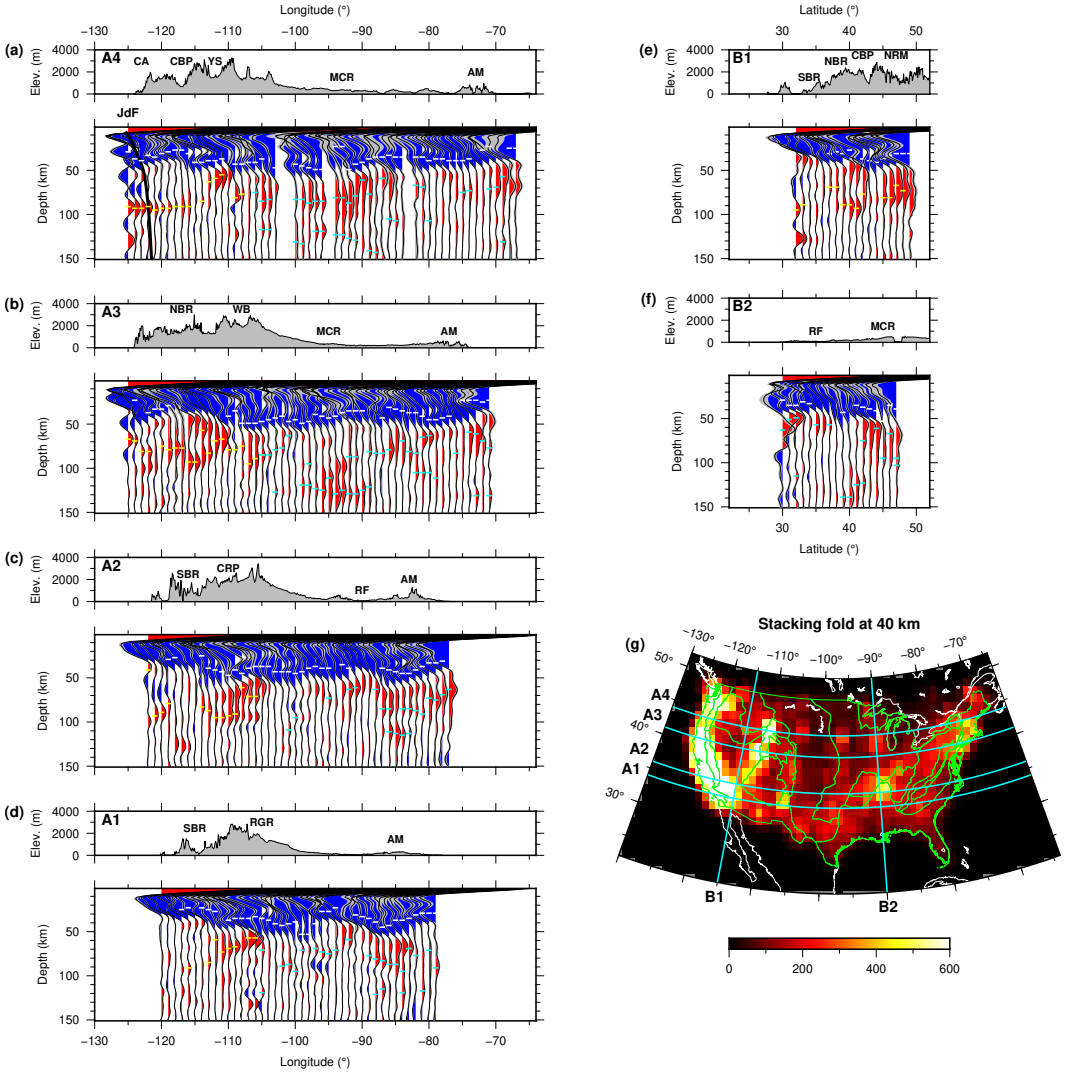

Figure 5. Results derived from our common-reflection-point (CRP) image. (a–d) W-E reflectivity and topography profiles along 34°(A1), 36° (A2), 41° (A3), and 44° (A4). Blue and red indicate impedance increasing and decreasing with depth, respectively. The uncertainty of each trace is marked in gray. Yellow and cyan bars: Our LAB picks in the Western US (WUS) and MLD picks in the Central and Eastern US (CEUS), respectively. Thick black curve: Juan-de-Fuca-slab interface (Hayes et al., 2018). Acronyms of important tectonic features: CA: Cascade Arc; CBP: Columbia Plateau; YS: Yellowstone Hotspot; MCR: Midcontinent Rift; AM: Appalachian Mountains; NBR: northern Basin and Range Province; WB: Wyoming Basin; SBR: southern Basin and Range Province; CRP: Colorado Plateau; RF: Reelfoot Rift; RGR: Rio Grande Rift; NRM: northern Rocky Mountain; JdF: Juan de Fuca Slab. (e) and (f): The same as (a–d), but S-N profiles along −115° (B1) and −90° (B2). (g): Stacking fold of our CRP image at 40 km depth. Major physiographic provinces of the US (Fenneman, 1946) are plotted in green in (g)

decreases with depth, respectively) and average the SRF model with the same $2^\circ \times 2^\circ$ grid cells used in our image.

The three images agree reasonably well for depth variations of the Moho, which appears as a positive arrival (impedance/velocity increase with depth) in the depth range 20–50 km (Fig. 6). Below the Moho, the profiles often do not agree very well in their details, but their average properties with depth appear similar. Each method shows significant negative arrivals between the Moho and ~ 100 km depth, although the SRF image is more diffuse, possibly because of its more limited depth resolution (Fig. 6). These negative arrivals indicate an impedance/velocity decrease with depth, which SRF studies have interpreted as the LAB in the Western and Eastern US and as an MLD in the Central US (e.g., Hopper and Fischer (2018)).

We note that the negative arrivals immediately below the Moho in our S reflection image are at least partly caused by the sidelobe of the Moho arrivals (Fig. S1). However, as we will discuss later, they are often stronger than one would expect from the Moho sidelobe alone. The SRFs have undergone deconvolution, but there has been some controversy regarding whether this process could nonetheless produce Moho-related sidelobe artifacts (e.g., Kind et al. (2020). Details of the arrivals between the Moho and 100 km appear more focused in depth in our S-reflection and PRF images, presumably due to their higher depth resolution, and are sometimes split into more than one apparent interfaces (Fig. 6). Between 100 and 150 km, our S reflection image has negative average arrivals, but these arrivals are generally weaker and less continuous than those seen at shallower depths (Fig. 6a). In contrast, the SRF image has a slightly positive average amplitude over this depth range, although there are occasionally negative amplitude features (Fig. 6b). Our PRF image over this depth range shows some strong features, especially in the west, but is likely contaminated by Moho multiples and thus is difficult to interpret (Fig. 6c).

Despite differences in resolution, our S-reflection image shows features similar to the other methods in some areas. For example, the negative arrival at ~ 130 km depth at $\sim -85^\circ$ appears consistent between our S-reflection image and the SRF image (Figs. 6a, b), and the multiple positive arrivals between 50 and 100 km beneath the Colorado Plateau appear very consistent between our S-reflection image and PRF image (Figs. 6a, c). We will now present more details of particular features in our S-reflection results.

3.2 Moho

We automatically pick the Moho from our data stack at each grid point as the strongest positive peak in the depth range of 20–60 km. In cases where the Moho is not the strongest positive peak in this depth range due to complicated crust and upper-mantle structure, we manually correct the Moho-depth picks to a more appropriate peak based on the Moho picks at adjacent grid points. The resulting Moho-depth map shows good correlation with physiographic provinces (Fig. 7a). The Moho is shallow (< 25 km) in the Basin and Range Province, the Columbia Plateau, the Gulf Coast, and the Atlantic Coast, whereas the Moho is deep in the Colorado Plateau, the southern Rocky Mountains, most of the Great Plains, and the Appalachian Mountains. We note that in areas where the Moho is extremely shallow, e.g., the southern Basin and Range, the Moho reflection arrives so early that it merges with the trailing side lobe of the reference pulse (direct S on the stacked trace), causing null Moho detections (Fig. 7).

The Moho amplitude also correlates well with the physiographic provinces, with high amplitude in the Basin and Range Province, the Columbia Plateau, the northern Rocky Mountains, the Gulf Coast, and the Atlantic Coast, and low amplitude in the Colorado Plateau, the middle Rocky Mountains, the Wyoming Basin, most of the Great Plains, and the Appalachian Mountains (Fig. 7b). Figure 7 compares these results with two previous Moho depth maps obtained using different methods: (1) the *Pn* analysis of Buehler

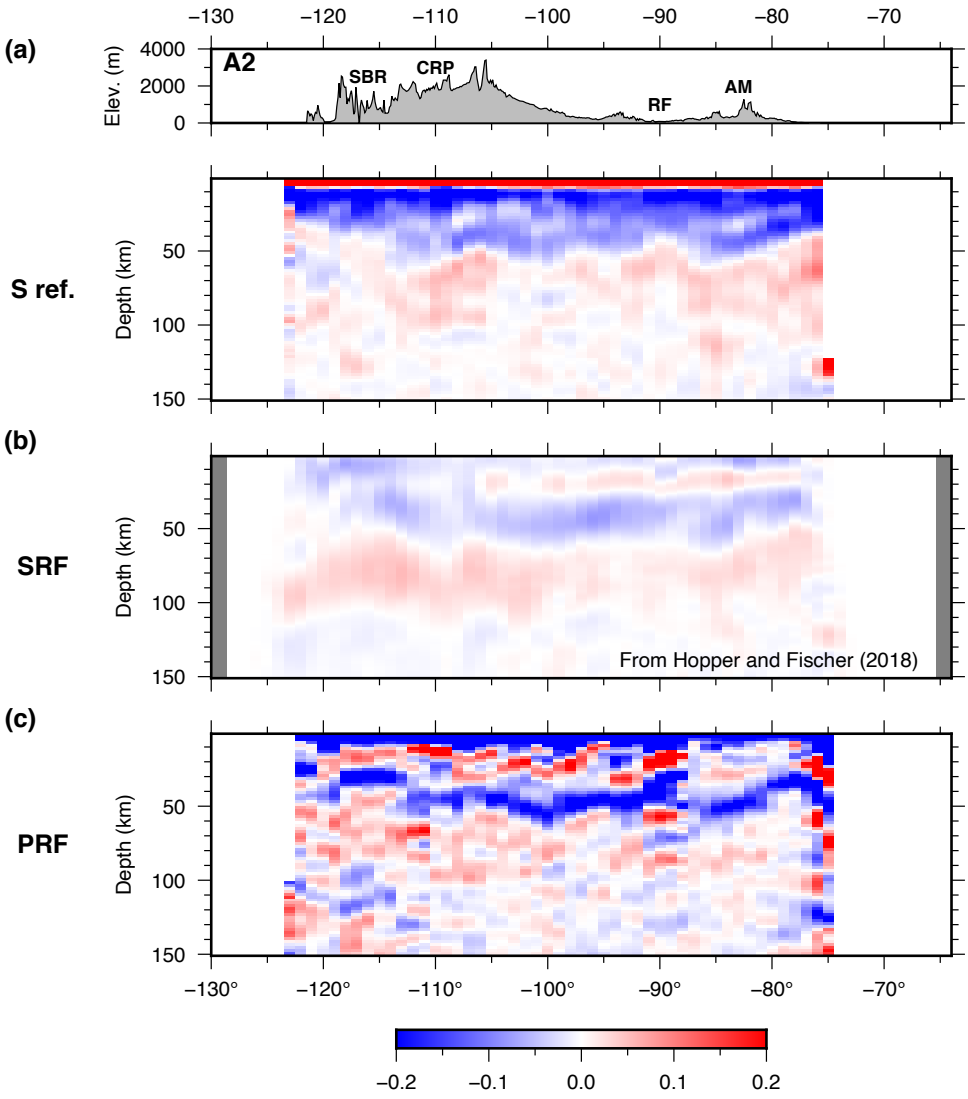

Figure 6. Comparison between (a) our S-reflection image, (b) SRF image from Hopper and Fischer (2018), and (c) our PRF image for Profile A2. Acronyms for key tectonic features are the same as in Fig. 5

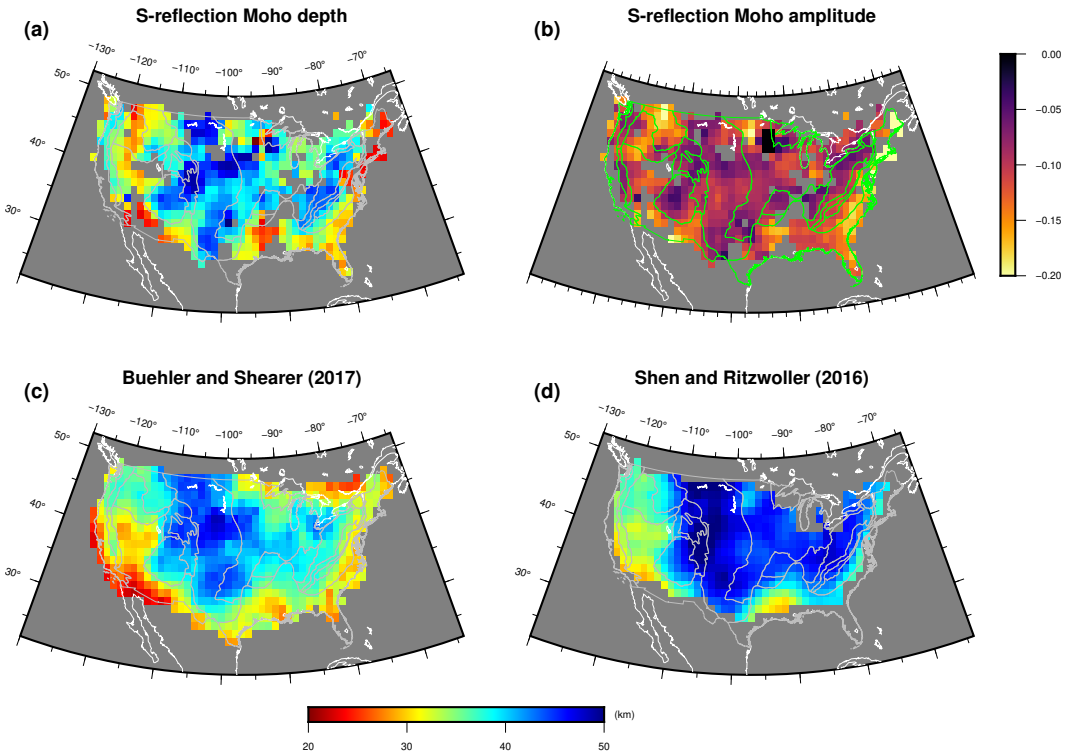

Figure 7. Comparison between our Moho observations and previous studies. (a) and (b) Moho depth and amplitude, respectively, from our S-reflection CRP image (c) Moho depth from Buehler and Shearer (2017). (c) Moho depth from Shen and Ritzwoller (2016).

and Shearer (2017), and (2) the joint surface-wave and PRF inversion of Shen and Ritzwoller (2016). The maps show reasonable agreement, particularly for the largest-scale features, which gives us some confidence that our method is capable of mapping shallow reflectors. However, we defer more detailed study of crustal structure for future work, preferring to focus here on imaging lithospheric structure, where our approach has perhaps its greatest potential advantages over other imaging methods.

3.3 Lithospheric discontinuities

On our S-reflection images, the mantle arrivals are predominantly negative (corresponding to NPRs) for both the Western US (WUS) and the Central and Eastern US (CEUS), although these arrivals appear stronger and more focused in the WUS than in the CEUS (Figs. 5a–f). In addition, we do not observe any NPR that extends across the whole continent, indicating that the NPRs in the WUS and the CEUS are likely unrelated features. Thus, we follow previous studies (e.g., Hopper and Fischer (2018)) to discuss our results in the WUS and CEUS separately. Because the deep events that we use in this study are better at imaging lithospheric structures compared to the shallow events used in Shearer and Buehler (2019), we will focus on discussing our images of the lithospheric discontinuities.

3.3.1 The lithosphere-asthenosphere boundary in the Western US

In the WUS, we observe a clear NPR in the depth range of 60–110 km on almost every trace of Profiles A1–A5 (yellow bars in Figs. 5a–e). Since most previous studies using SRFs also showed a negative interface in this depth range, which was commonly

interpreted as the LAB in the WUS (e.g., Hopper and Fischer (2018), L. Liu and Gao (2018), and Kind et al. (2020)), we adopt their interpretation and search for the strongest negative peak between the Moho and 110 km in our CRP image volume to evaluate the depth and amplitude variation of the LAB in the WUS. When the strongest negative peak is within 30 km of the Moho, a depth range that also contains the Moho sidelobes, we identify the peak as the LAB only when it satisfies both of the following criteria: First, its amplitude exceeds 0.5 of the Moho amplitude, and second, its amplitude is more than two times stronger than the strongest negative peak in the depth range below it. Otherwise, we will instead identify the strongest negative peak in the depth range below this peak as the LAB. An example of grid cells with negative peaks immediately below the Moho that satisfies both criteria is the grid cell at the Yellowstone Hotspot ($\sim -112°$ on Profile A4; Fig. 5a), where the NPR at ~ 55 km depth is almost as strong as the Moho and is clearly the most prominent NPR in the mantle. At some grid cells, the strongest negative peak is within 30 km of the Moho and is stronger than 0.5 of the Moho amplitude, but is not more than two times stronger than the strongest negative peaks below it (e.g., the Colorado Plateau, $\sim -110°$ on Profile A2; Fig. 5c). We term these grid cells as having ambiguous LAB picks (Fig. 5c) because at these locations the NPRs immediately below the Moho usually have comparable amplitude to a deeper NPR, making the identification of the LAB difficult. Furthermore, we treat only LAB picks with amplitude > 0.02 as robust observations and show their depths in Fig. 5a.

Our LAB depth and amplitude maps show interesting correlations with physiographic provinces (Figs. 8a, b). The areas with the strongest LAB amplitudes are: (1) The eastern border of the Colorado Plateau, including the Rio Grande Rift and the boundary between the Colorado Plateau and the southern Rocky Mountains, and (2) the northern Rocky Mountains (Fig. 8b). These areas also have the shallowest LAB in the WUS (< 70 km; Fig. 8a). The areas with moderate LAB amplitudes are: (1) Most of the Colorado Plateau, (2) the northern Basin and Range Province, and (3) most of the Pacific Coast, including the Cascade Arc and northern and central California (Fig. 8b). The LAB in these areas generally has a moderate depth (between 80 and 90 km; Fig. 8a). The LAB in the northern Basin and Range Province clearly shallows from ~ 90 km at the center to ~ 70 km at its western and eastern boundaries, namely the Sierra Nevada Transition Zone and the Wasatch Fault Zone (Figs. 8a and 5b), where GPS observations have shown concentrated crustal extension (e.g., Hammond et al. (2014), Thatcher et al. (1999), and Martinez et al. (1998)). The areas with a weak LAB are: (1) Most of the Columbia Plateau, (2) the southern Basin and Range Province, and (3) southern California (Fig. 8b). Many grid points in these areas do not show LAB-depth values because their LAB amplitudes are < 0.02 (Fig. 8a). The Death Valley Fault Zone, which marks the western boundary of the southern Basin and Range Province, also appears to show a shallower LAB than the surrounding area (Fig. 8a), although the generally low LAB amplitudes in the southern Basin and Range Province renders this observation less robust than the LAB shallowing at the boundaries of the northern Basin and Range Province. The two main areas with ambiguous LAB picks are the northern Basin and Range Province and the southern Rocky Mountains (Fig. 8c). These areas likely have more than one significant velocity drop below the Moho. For example, the strong negative peaks following the Moho peaks in the northern Basin and Range Province suggest the presence of a NPR immediately below the Moho at ~ 45 km in addition to the LAB picked at ~ 90 km (Figs. 5b, e). To confirm the presence of this sub-Moho NPR requires detailed waveform modeling to account for the sidelobe amplitudes of the local reference pulses, which is beyond the scope of this study. We will nonetheless present PRF observations that also suggest the presence of a sub-Moho negative velocity gradient zone in the northern Basin and Range Province in Section 4.1

Since the free-surface-Moho double reflection (hereafter "Moho double reflection") has a positive polarity and arrives at a similar time window to our LAB (Fig. 1), it might be misidentified as the LAB. To assess this possibility, we plot the Moho depth and am-

plitude against the LAB depth and amplitude for each grid point in the WUS, and find little correlation (Figs. 9a, b), making it unlikely that our LAB observations are caused by Moho double reflections.

We note that the depth variations of our LAB in Figure 8 do not agree very well with the depth maps of negative-velocity-gradient features in the WUS previously obtained from SRF studies (e.g., Figure 3 from L. Liu and Gao (2018) and Figure 5 from Hopper and Fischer (2018)). We focus here on comparisons to Hopper and Fischer (2018) and plot a depth and amplitude comparison obtained by averaging the LAB depths and amplitudes from Hopper and Fischer (2018) within our grid cells (Fig. S4). The SRF LAB depth distribution shows a different pattern from our results and also generally has less depth variation (Figs. S4a, b). For example, our LAB is extremely shallow (< 70 km) in the Rio Grande Rift, whereas the SRF LAB has a moderate depth ~ 80 km in the region (Figs. S4a, b). Another example is the Cascade Arc, where our LAB (~ 90 km deep) is significantly deeper than the SRF LAB (~ 75 km deep). Despite these differences, our results seem to agree with the SRF results on the shallowing of the LAB near the western and eastern boundaries of the northern Basin and Range Province, though our results show more shallowing in the east, whereas the SRF results show more shallowing in the west (Figs. S4a, b). The SRF LAB amplitude generally lacks strong variations, with a slightly stronger LAB in the Basin and Range Province and the northern Rocky Mountains, which is also different from our LAB amplitude distribution. We note that although we use Hopper and Fischer (2018) to represent previous SRF studies here, the results from these studies can differ significantly in certain areas, which likely explains some of the discrepancies between our results and the SRF results from Hopper and Fischer (2018). For example, Levander and Miller (2012) found a LAB depth of $\sim$ 65 km in the Rio Grande Rift, significantly deeper than ~ 80 km given by Hopper and Fischer (2018) and much closer to our result ($\sim$ 60 km). We will further discuss possible reasons for discrepancies between our results and previous studies in Section 4.2.

3.3.2 Mid-lithospheric discontinuities in the Central and Eastern US

In the CEUS, we generally observe two bands of negative arrivals between the Moho and 100 km depth and between 100 km and 150 km depth (Figs. 5a–d and f). Since these NPRs are within the high-velocity lithosphere shown by seismic tomography studies in the CEUS (e.g., H. Zhu et al. (2017)), we term them MLDs, in contrast to the LAB in a similar depth range in the WUS. Because the NPRs in these two depth ranges sometimes have comparable amplitude (e.g., $\sim -85°$ on Profile A2; Fig. 5c), we define two MLDs in these two depth ranges (hereafter "shallow MLD" and "deep MLD"). This definition also makes our shallow MLD directly comparable to MLDs found by previous SRF studies, which are mostly in the depth range between the Moho and 100 km depth (e.g. Hopper and Fischer (2018); Figs. S5b, d). To pick the shallow MLD, we follow the same procedure as picking the LAB in the WUS because this depth range also contains Moho sidelobes. For the deep MLD, we simply pick the strongest negative peak between 100 km and 150 km depth. Similar to our treatment of LAB picks, we only show MLD depths at locations where their amplitudes are > 0.02. Although we define our two MLDs based on their depth ranges, we do not preclude the possibility that they may represent the same interface in some areas. For example, on Profile B2, the two MLDs may be two parts of one interface that dips southward between 35° and 45° (Fig. 5f). Since our data coverage in the CEUS is usually insufficient for us to determine if our two MLDs are spatially connected, we will treat them as separate features in this study, while leaving discussions of their detailed geometries to future studies.

Our results show that the shallow MLD generally has a higher amplitude than the deep MLD, with the amplitude of both MLDs varying greatly across the CEUS (Figs. 10c, d). The amplitude of the shallow MLD is highest in the northern Midcontinent Rift, where it is at 70–80 km depth (Figs. 10a, c and 5a). Another area where the shallow MLD

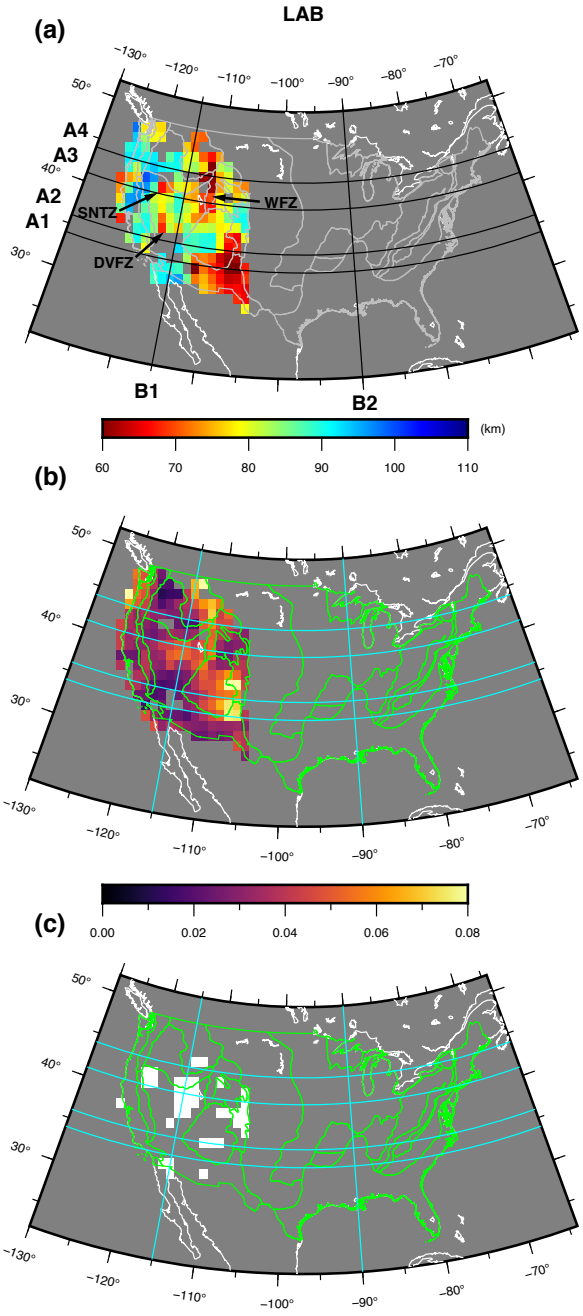

Figure 8. Depth and amplitude map of our LAB in the WUS. (a) LAB depth in the WUS. SNTZ: Sierra Nevada Transition Zone; WFZ: Wasatch Fault Zone. DVFZ: Death Valley Fault Zone. (b): LAB amplitude in the WUS. (c) Regions with ambiguous LAB depth picks.

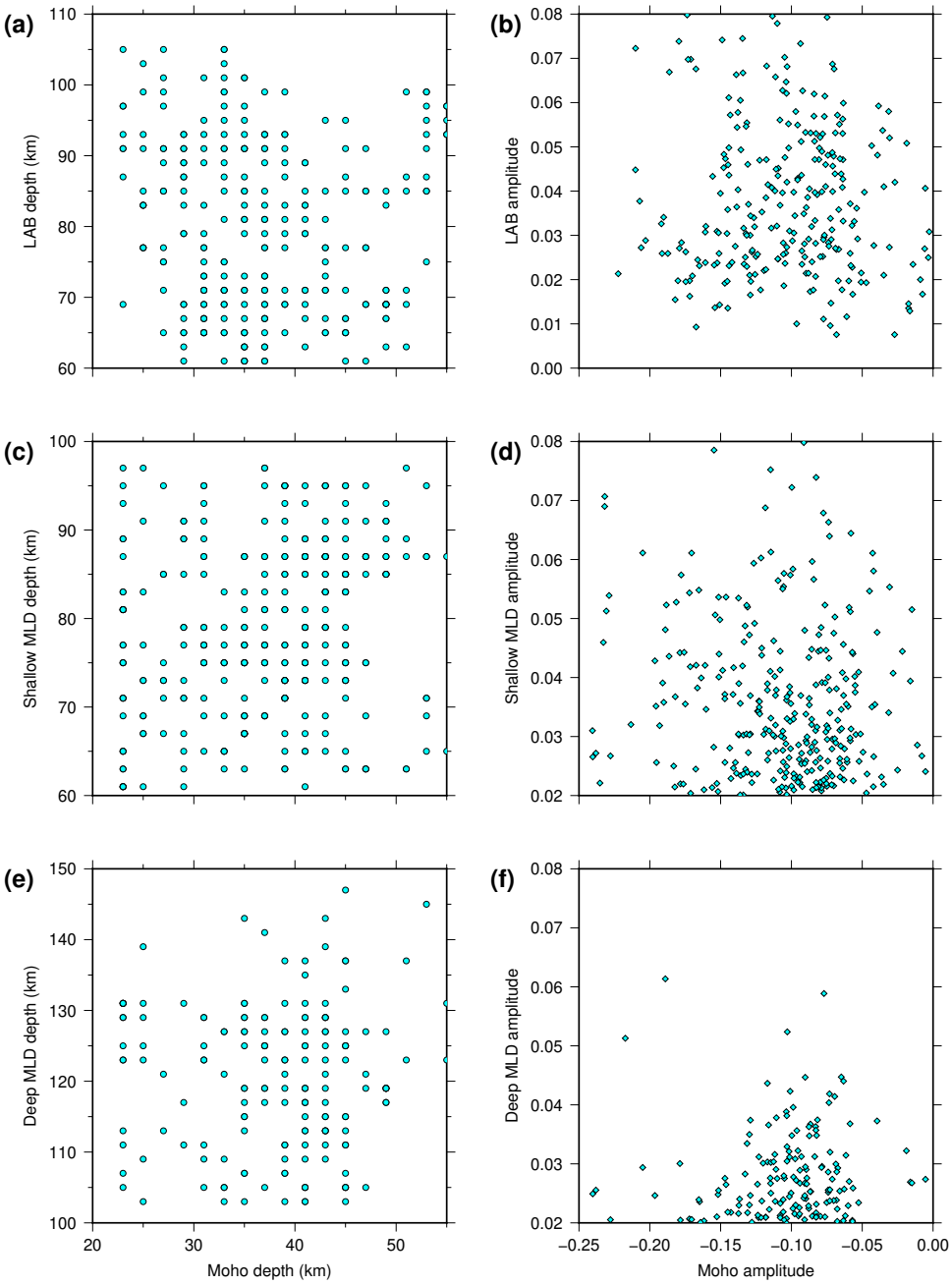

Figure 9. Cross plots of Moho amplitude and depth against the amplitude and depth of the LAB in the WUS and the MLDs in the CEUS. (a) Moho and LAB depth in the WUS. (b) Moho and LAB amplitude in the WUS. (c) Moho and shallow-MLD depth in the CEUS. (d) Moho and shallow-MLD amplitude in the CEUS. (e) Moho and deep-MLD depth in the CEUS. (f) Moho and deep-MLD amplitude in the CEUS.

is strong is the area including the Reelfoot Rift and the southern Appalachian Mountains (Figs. 10a, c). The MLD beneath the flanks of the Reelfoot Rift is very shallow (< 70 km), whereas the MLD beneath the southern Appalachian Mountains is deep ($>$ 80 km)(Figs. 10a, c and 5c, d). The deep MLD is strong in the southern Midcontinent Rift, where it is $\sim$ 125 km deep, and the western foothills of the Appalachian Mountains, where it is ~ 115 km deep. We also plot the depth and amplitude of our MLDs against the Moho depth in the CEUS and find little correlation (Figs. 9c–f), indicating that our MLD observations are unlikely due to Moho sidelobes or Moho double reflections. Interestingly, our shallow and deep MLDs appear to have strong amplitudes in the same (e.g., the southern Appalachian Mountains) or adjacent regions (e.g., the southern and northern Midcontinent Rift), which implies that the two MLDs may be related features. We will further discuss this possibility in Section 4.3.

In the CEUS, our shallow MLD is in the same depth range as the maximum negative-velocity gradient (NVG) from Hopper and Fischer (2018), which was interpreted as an MLD in the Central US and the LAB in the Eastern US. We thus compare the amplitude and depth distribution of our shallow MLD with those from Hopper and Fischer (2018) averaged within our grid cells (Fig. S5). In the Reelfoot Rift and the southern Appalachian Mountains, our MLD shows similar depth variation to the SRF MLD (shallow in the Reelfoot Rift and deep in the southern Appalachian Mountains), although our MLD in the Reelfoot Rift (< 65 km deep) is significantly shallower than the SRF MLD (~ 75 km deep)(Figs. S5a, b). In the northern Midcontinent Rift, our MLD is at similar depth as the SRF MLD (between 70 and 80 km depth)(Figs. S5a, b). A major difference between our shallow MLD and the SRF MLD is that our MLD shows strong amplitude variation, whereas the SRF MLD has a relatively uniform amplitude (Figs. S5c, d). For example, our shallow MLD is weak in most of the Great Plain, whereas the SRF MLD in this area has similar amplitude as in the rest of the CEUS. We will further discuss possible reasons for this discrepancy in Section 4.3.

4 Discussion

4.1 Comparison with PRF results

Although PRF and SRF have similar sensitivity to elastic parameter changes across discontinuities, studies of lithospheric discontinuities using PRF and SRF have not always yielded consistent results (e.g., Levander and Miller (2012) and S. M. Hansen et al. (2015)). As discussed above, although we observe NPRs within a similar depth range to those seen in SRF studies, the depths and locations of specific features do not agree very well. Some of these differences may be related to the broader depth resolution of the SRF compared to our S-reflection method, so it is worthwhile also comparing our images with PRF results, which should have depth resolution closer to our images than that of SRFs. Thus, we compare our S-reflection CRP images with our PRF CCP images along our four W-E profiles A1–A4 and two S-N profiles B1 and B2 (Figs. 11 and 12). To estimate the depth range where we expect the interference of Moho *PpPs*, we also compute the predicted depths of Moho *PpPs* for each trace using the local Moho depth and an average crustal V_p/V_s ratio of 1.73 (gray diamonds in Figs. 11 and 12).

We observe good agreement between the variation trend of the S-reflection Moho depth and PRF Moho depth along all the profiles, though the absolute Moho depth can be off by up to 10 km (Figs. 11 and 12), likely because we did not account for variations in average crustal V_p/V_s ratio (both our S-reflection and PRF images are computed using the IASP91 model). The PRF traces show sharper Moho arrivals and more detailed crustal structures because the PRFs are filtered at much higher frequency than our S reflection traces.

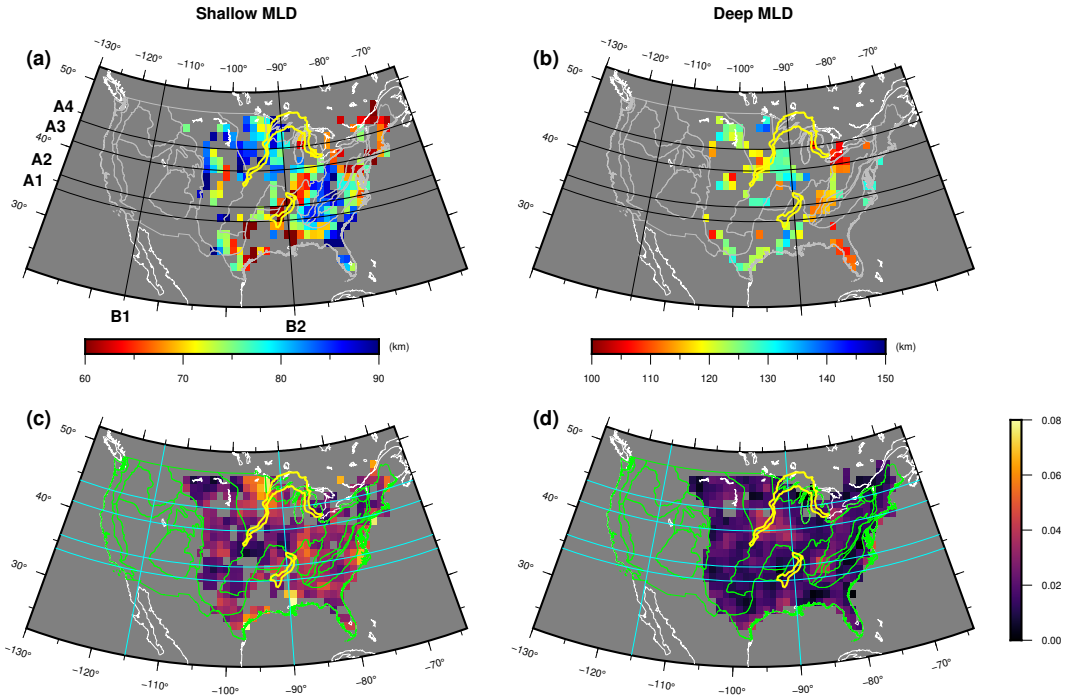

Figure 10. Depth and amplitude maps of our shallow MLD and deep MLD in the CEUS. (a) and (b): Depth maps of our near-Moho MLD and deep MLD in the CEUS, respectively. Only grid points with MLD amplitude > 0.02 are shown in (a) and (b), respectively. (c) and (d): Amplitude maps of our near-Moho MLD and deep MLD in the CEUS, respectively.

Below the Moho, our PRF images also show similar features to our S-reflection images in many areas. On Profile A1, both images show clear negative interfaces between 50 and 90 km beneath the southern margin of the Colorado Plateau and the Rio-Grande Rift (Fig. 11a). We also observe negative interfaces at $\sim$ 75 km depth beneath the Appalachian Mountains on Profile A1 of both methods (Fig. 11a). On Profile A2, the multiple negative interfaces beneath the Colorado Plateau appear very consistent between the two images. In addition, similar to Profile A1, both images show negative interfaces below the Appalachian Mountains on Profile A2 remove[authors], which includes both the shallow and deep S-reflection MLD in the area, though the PRF interfaces appear significantly weaker (Fig. 11b). On Profile A3 both images show the shallowing of the negative interface beneath the western boundary of the northern Basin and Range Province (the Sierra Nevada Transition Zone), although this feature appears to be more coherent on the PRF image (Fig. 11c). In the center of the northern Basin and Range Province, the strong Moho sidelobe on the S-reflection image and the clear negative arrival immediately below the Moho on the PRF image both suggest the presence of a sub-Moho negative interface at $\sim$ 50 km depth, in addition to the LAB imaged by S reflections at $\sim$ 85 km depth (Fig. 11c). In addition, we observe negative interfaces between 60 and 90 km depth beneath the central Rocky Mountains on both images (Fig. 11c). We also observe negative interfaces beneath the western foothills of the Appalachian Mountains between 80 and 100 km depth on Profile A3 of both methods (Fig. 11c). Moving further north, on Profile A4, both images show strong negative arrivals at $\sim$ 90 km beneath the subducting Juan de Fuca slab (Fig. 11c). This arrival is less coherent on the PRF image for two possible reasons: First, the PRFs have more high-frequency content than the S-reflection data, making them more sensitive to small-scale lateral variation of this negative interface. Second, multiple reflections at shallow interfaces between the slab and the upper

plate may further complicate the PRF image (R. T. Hansen et al., 2012). Similar to Profile A1–A3, on Profile A4, we observe negative interfaces beneath the Appalachian Mountains between 60 and 90 km on both images (Fig. 11d).

On Profile B1, the negative interface between 80 and 90 km beneath the northern Basin and Range Province and northern Rocky Mountains appear very consistent between the two images (Fig. 12a).In the northern Basin and Range Province, similar to Profile A3, both images suggest the presence of a sub-Moho negative interface at ~ 50 km in addition to the LAB at~ 85 km (Fig. 12a). Besides, the broad negative S-reflection interface beneath the northern Rocky Mountains on this profile likely includes both the PRF interfaces at ~ 80 and ~ 60 km depths (Fig. 12a). The similarity between the two images on Profile B2 is not as obvious as on the other profiles, but the two images still agree on the presence of negative interfaces beneath the Midcontinent Rift in the depth range of 60–90 km (Fig. 12b).

Two main factors may contribute to the discrepancies between our S-reflection and PRF results. First and most importantly, Moho *PpPs* and the other Moho multiples could interfere with *Ps* from lithospheric discontinuities, which is also the primary reason that PRFs are less popular than SRFs in studying lithospheric structure. As shown in the above comparison between S-reflection and PRF results, the agreement between them is significantly better in the top 100 km, a depth range generally free of the interference of Moho multiples (The first Moho multiple, Moho *PpPs*, is mapped to > 100 km depth on most traces; Figs. 11 and 12). In addition, multiples generated by intra-crustal interfaces may also interfere with *Ps* from lithospheric discontinuities (e.g., Fig. 1), though their effects should be less pronounced than the Moho multiples. Second, significant changes in anisotropy properties may be present at some lithosphere discontinuities, causing these discontinuities to have distinctly different behavior for S-reflections and PRFs. We will discuss the effects of anisotropy in more detail in Section 4.2.

The general agreement between our S-reflection and PRF images not only helps validate our methodology but also implies the potential of joint analyses between the two methods. Because lithospheric discontinuities are generally weak and subject to contamination from Moho multiples and other phases, the presence of a discontinuity on both S-reflection and PRF results is strong evidence for the existence of the interface. Moreover, since S-reflections and PRFs contain seismic responses for two independent systems, SH and P-SV, a joint analysis of them could better constrain the anisotropic properties of a discontinuity, though this analysis will require good event-azimuth coverage and may only be applied to depth ranges free of PRF Moho multiples (e.g., < 100 km for the contiguous US). In addition, jointly analyzing Moho S-reflections and Moho *Ps* could constrain the average crustal V_p/V_s ratio, a key parameter closely related to average crustal composition (Yuan, 2015; T. Liu et al., 2019), in a similar way to the classic $H-\kappa$ stacking technique (L. Zhu & Kanamori, 2000). A potential advantage of this method is that it does not rely on the PRF Moho multiples, which are not always reliably observed. The application of this analysis may require the S-reflection data to be filtered to higher frequency than used in this study, for example to a similar frequency band as typically used for SRF studies (Fig. 1), which would be more suitable for studying crustal structures.

4.2 Nature of the LAB and its relation with active tectonics in the Western US

The nature of the LAB can only be reliably resolved with joint constraints from different seismic observations. One feature in the WUS that is consistently shown by different seismic methods is the significantly shallowing of the LAB at the western and eastern boundaries of the northern Basin and Range Province (Figs. 5b, 8a, 11, and S4a, b; Hopper and Fischer (2018), S. M. Hansen et al. (2015)), which is consistent with GPS observations that extension in the northern Basin and Range Province mostly occurs on

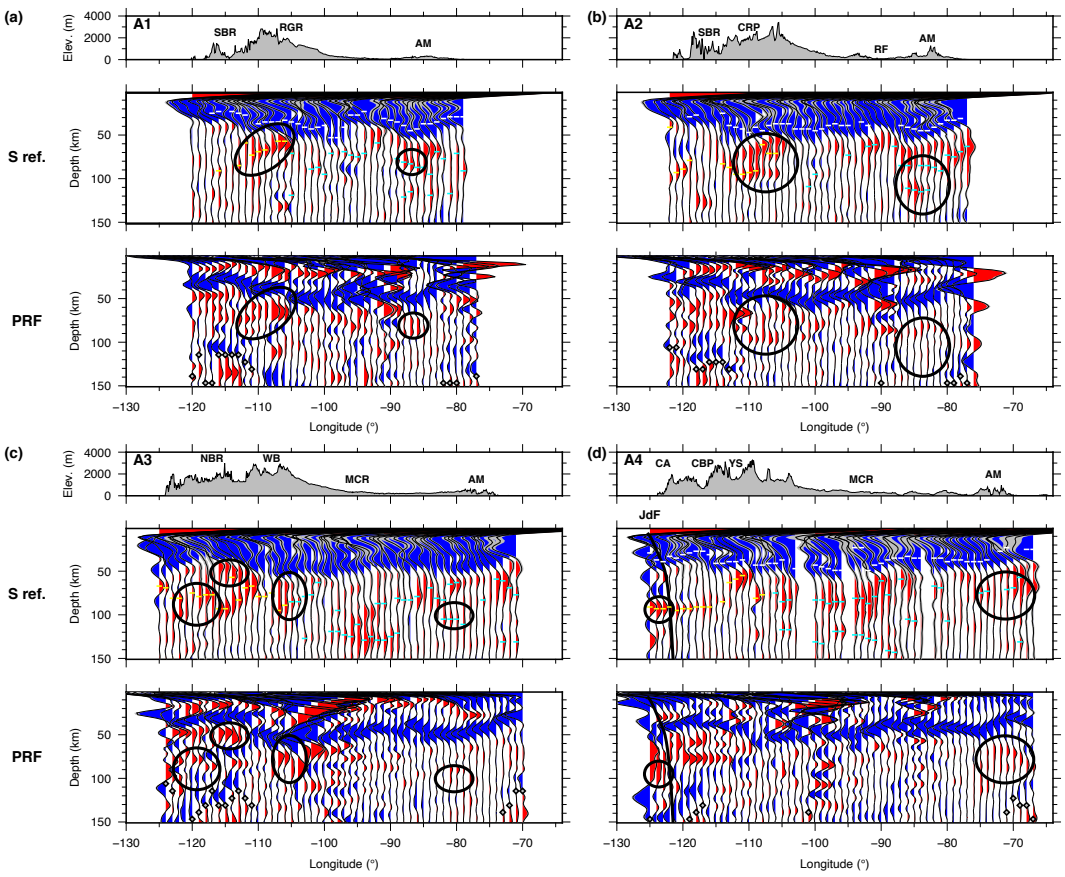

Figure 11. Comparison between our S-reflection results and our PRF common-conversion-point (CCP) image computed with the EARS PRFs along Profiles A1–A4. On both the S-reflection and the PRF traces, blue indicates velocity or impedance increasing with depth and red indicates velocity or impedance decreasing with depth. The parts of the profiles where S reflections and PRFs show similar structures are circled in black. Gray diamonds: predicted depths of Moho *PpPs*. The interface markers and acronyms of key tectonic features are the same as in Fig. 5

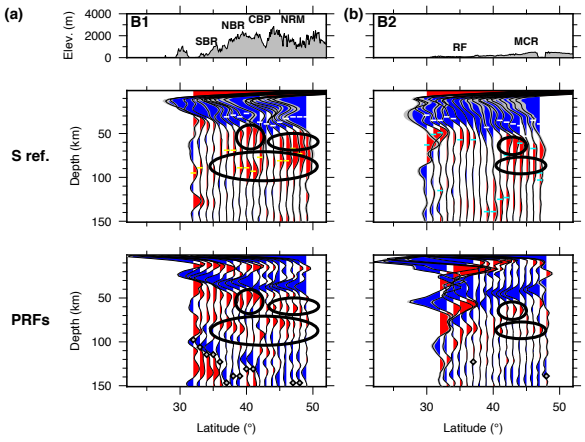

Figure 12. The same as Fig. 11, but for Profiles B1 and B2.

its eastern and western boundaries (e.g., Hammond et al. (2014), Thatcher et al. (1999), and Martinez et al. (1998)). In particular, Thatcher et al. (1999) and Martinez et al. (1998) found concentrated extension at the Sierra Nevada Transition Zone and the Wasatch Fault Zone, where we also observe significant lithospheric thinning (Figs. 5b and 8a). Interestingly, the lithospheric thickness in the northern Basin and Range Province seems to be inversely correlated with the crustal thickness, which is greater near the edges than in the center (Figs. 5b and 7a, c). If we regard the crustal thickness in the northern Basin and Range Province as a measure of cumulative past lithosphere extension, this suggests that active tectonic processes, as opposed to past ones, likely control the characteristics of the LAB in the northern Basin and Range Province. Another interesting feature consistently shown by our S-reflection and PRF images in the WUS is the strong negative interface at ~ 90 km beneath the Juan de Fuca slab (Fig. 11d), which might represent a sharp velocity drop at the top of a strong low-velocity anomaly beneath the slab recently revealed by seismic tomography studies (e.g., Hawley et al. (2016)). Moreover, our S-reflection and PRF images suggest the presence of negative interfaces immediately below the Moho in some parts of the WUS, which are usually a separate interface significantly shallower than the local LAB (e.g., the northern Basin and Range Province; Figs. 11e and 12a). This observation is supported by recent *Pn* analyses, which found a predominantly negative vertical velocity gradient in the uppermost mantle beneath the WUS (e.g., Buehler and Shearer (2017)). Further studies are needed to confirm the presence of these shallow negative interfaces and to understand the upper-mantle structure of these areas, which likely cannot be described with a simple lithosphere-over-asthenosphere model.

Similar to agreements between different seismic observations, disagreements between different seismic observations could also shed light on the nature of the LAB. The most outstanding discrepancy between our S-reflection results and previous seismic studies on the LAB of the WUS is our weak LAB amplitude in the southern Basin and Range Province and the Columbia Plateau (Fig. 8a), where previous studies using PRF and SRF have largely found strong LAB conversions (e.g., Hopper and Fischer (2018) and Levander and Miller (2012)). In addition, our PRF images also show clear negative converters in the mantle beneath the southern Basin and Range Province and the Columbia Plateau, where the S-reflection images generally have low amplitude (Figs. 11a, b, d and 12a). Specifically, Fig. 12a shows that as the S-reflection LAB amplitude diminishes southward beneath the Basin and Range Province, the PRF amplitude stays strong. A plausible explanation for this discrepancy between S-reflection observations and receiver-function observations is that the LAB in the southern Basin and Range Province and the Columbia Plateau has a significantly greater drop in V_{SV} than V_{SH}, which generates strong receiver-function conversions but only weak SH reflections. This type of velocity drop can be caused by a melt-rich layer at the base of the lithosphere where the melt is segregated into sub-horizontal bands due to horizontal shear at the LAB (B. K. Holtzman & Kendall, 2010; Kawakatsu et al., 2009). In Kawakatsu et al. (2009), this mechanism was invoked to explain the strong receiver-function conversions at the oceanic LAB. Both the southern Basin and Range Province and the Columbia Plateau have abundant recent magmatic activities, which supports our hypothesis. Furthermore, with a joint seismic-petrologic analysis, Plank and Forsyth (2016) suggested the ponding of melt at the base of the lithosphere in the southern Basin and Range, which agrees with our model. A detailed modeling of S-reflection and receiver-function waveforms in the southern Basin and Range Province and the Columbia Plateau that accounts for effects of anisotropic mediums is clearly needed to further evaluate our hypothesis and constrain the nature of the LAB in these two areas, which is beyond the scope of this paper.

A further question is why some areas show a clear LAB on both our S-reflection and receiver-function images (e.g., the northern Basin and Range Province), whereas other areas only show a clear LAB on receiver-function images (e.g., the southern Basin and Range Province and the Columbia Plateau). If we assume that sub-horizontal melt-rich shear bands are responsible for the areas with low S-reflection LAB amplitudes, a dif-

ferent mechanism is needed for areas with both strong S-reflection LAB and receiver-function LAB. One possibility is that the melt at the base of the lithosphere in these areas is uniformly distributed rather than segregated into shear bands, which would cause an isotropic velocity drop. A potential problem of this model is that if melt is present under the condition of strong horizontal shear, a realistic condition at the base of the plates, it will tend to segregate into shear bands, rendering a uniform melt distribution unlikely (B. Holtzman et al., 2003; Katz et al., 2006). Another possibility is that mechanisms other than melt are responsible for the LAB in many areas in the WUS. One such mechanism is elastically accommodated grain-boundary sliding, which could generate sharp velocity drops at the LAB given high but sub-solidus temperature and high water content (Karato, 2012; Karato et al., 2015). This model could explain the presence of strong S-reflection LAB and receiver-function LAB in areas with no recent magmatic activities (e.g., the northern Rocky Mountains; Fig. 12a). In summary, our results suggest that different mechanisms are likely responsible for the LAB in different areas of the WUS.

Due to limitations of our waveform-modeling capacity at this stage, our interpretations of the LAB in the WUS are largely qualitative. Another constraint of our current analysis is the large bin size ($2^\circ \times 2^\circ$) of our CRP images, which is necessary for addressing our uneven data coverage but makes it difficult for our images to resolve rapid lateral variations of lithospheric structure. Future studies that apply anisotropic waveform-modeling to S-reflection and receiver-function data collected in areas with good data coverage will likely provide better constraints on the nature of the local LAB.

4.3 Existence of MLDs in the Central and Eastern US

The existence of MLDs in the Central US is much debated, with different SRF studies presenting distinct results. Using similar techniques, Hopper and Fischer (2018) and L. Liu and Gao (2018) agreed that an MLD is present in the depth range of 70–100 km in the Central US. In contrast, Kind et al. (2020) argued that the MLD in the Central US shown in Hopper and Fischer (2018) and L. Liu and Gao (2018) is largely an artifact caused by the Moho sidelobe. The shallow MLD in our results is approximately in the same depth range as the MLD from the SRF studies (Hopper & Fischer, 2018; L. Liu & Gao, 2018) and thus might represent the same interface. However, our shallow MLD shows strong amplitude variation and may only exist in spatially isolated areas, unlike the nearly ubiquitous MLD shown by previous SRF studies (Hopper & Fischer, 2018; L. Liu & Gao, 2018). If we assume that the MLDs in the CEUS represent primarily isotropic velocity drops, i.e., they have similar manifestations on S-reflection and receiver-function observations, our results suggest that MLDs are only present in limited areas in the CEUS, a model between the two end-member models proposed by Hopper and Fischer (2018) (ubiquitous MLD) and Kind et al. (2020) (no MLD). The discrepancy between our MLD model and the two end-member models could be explained by limitations of the two studies: The results of Hopper and Fischer (2018) might have suffered the sidelobe problem as suggested by Kind et al. (2020), whereas Kind et al. (2020) may have failed to resolve local negative interfaces due to the heavy lateral smoothing that they used or the inherent low depth and lateral resolution of SRFs. Our S-reflection observations of the shallow MLD is supported by our PRF images, which also only show clear negative interfaces between the Moho and 100 km depth in limited areas, mostly regions where our S-reflection images also show strong shallow MLDs (Figs. 11 and 12). In addition, *Pn* analyses also showed primarily positive uppermost-mantle vertical velocity gradients in the CEUS, except for a few regions with negative gradients, which include the northern Midcontinent Rift and the Reelfoot Rift (Buehler & Shearer, 2017), where our S-reflection images also show the strongest shallow MLD (Fig. 10a). In summary, our results and previous seismic studies suggest that MLDs above 100 km depth are likely local as opposed to ubiquitous features in the CEUS.

In our S-reflection images, grid cells with strong shallow MLDs and deep MLDs are mostly located in two regions: the Midcontinent Rift and the area consisting of the Reelfoot Rift and the southern Appalachian Mountains (Figs. 10c, d). Our PRF images also generally show negative convertors in these two areas, especially beneath the Appalachian Mountains (Fig. 11). Because the Midcontinent Rift, the Reelfoot Rift, and the southern Appalachian Mountains have all undergone major tectonic events in the past (failed rifting in the two rifts and continental collision in the southern Appalachian Mountains), we speculate that the MLDs in the CEUS may be related to compositional changes caused by past lithosphere modifications. Karato et al. (2015) proposed elastically accommodated grain-boundary sliding as a mechanism for MLDs beneath stable continents. However, their model predicts a ubiquitous MLD beneath continents, which is inconsistent with our observations. Since the CEUS is generally less well sampled by our dataset compared with the WUS (Fig. 5g), future studies incorporating data from local temporary arrays are needed to uncover more details of the MLDs in the CEUS, especially in the areas with strong evidence of their presence, e.g., the Midcontinent Rift and the southern Appalachian Mountains.

4.4 How can we best resolve lithospheric structure?

Here, we introduce a new method for imaging lithospheric structure that analyzes topside multiples from teleseismic SH waves generated by deep earthquakes, and apply it to data from TA and other networks in the contiguous United States. The use of deep earthquakes removes the ambiguity between source- and receiver-side lithospheric reflections that complicated the earlier TA study of Shearer and Buehler (2019). Our new approach indeed produces images significantly different from Shearer and Buehler (2019). For example, our LAB in the WUS has a very different depth distribution from the NPR shown in Figure 10 of Shearer and Buehler (2019), which was picked in a similar depth range as our LAB. We believe that our results about lithospheric discontinuities are superior to those from Shearer and Buehler (2019) because our new approach significantly reduces artifacts due to the source-receiver ambiguity in Shearer and Buehler (2019). Our method has similarities to standard reflection seismology techniques, including common-reflection-point stacking. However, the distribution of deep earthquakes is much sparser, particularly in azimuth, than the source distribution of typical controlled-source reflection experiments, which reduces the robustness of our results. Thus, although we use the term "image" throughout this paper to refer to reflectors defined by peaks in the waveform stacks, some caution is warranted because some of these features might be artifacts caused by scattering from 3D structures more complex than the simple horizontal layering that common-reflection-point stacking implicitly assumes. This is also a concern for receiver-function methods, which also generally suffer a non-uniform source distribution. Note that the uncertainty introduced by possible scattered arrivals is distinct from the question of the statistical significance of the peaks in the waveform stacks, which can be assessed using bootstrap resampling or other methods. These formal statistical uncertainties generally become quite low when the stacking fold is large, but this does not address the issue as to whether the seismic waves generating a peak are coming from the assumed common-reflection-point (or common-conversion-point) region or somewhere else.

Ideally, these imaging uncertainties could be reduced through more advanced reflection seismology methods, such as migration, but these methods perform best with uniform source and receiver distributions, which are difficult to achieve with natural seismicity and most existing seismic networks. Given these limitations, how can we best assess the reliability of our results for lithospheric structure? A reasonable approach is to focus on those features that are seen in more than one type of analysis, i.e., our topside reflection approach compared to P- and S-receiver functions. In this study, the best agreement between all three methods is seen in the largest scale features. For example, considering average continent-scale structures, the depth range between about 60 and 100

depth is characterized by velocity drops with depth that are strong enough to be imaged with all three methods (e.g., Fig. 6). This is seen for both the western and eastern United States and is a very consistent and robust result. However, as discussed above, at finer scales we find much better agreement between our results and PRF images than with SRF images. This discrepancy is somewhat surprising because SRFs are generally considered superior to PRFs for resolving lithospheric interfaces, as they are free of contamination from crustal multiples. However, as discussed earlier, a depth range exists below the Moho *Ps* and the earliest Moho reverberation Moho *PpPs* (Moho to $\sim$ 100 km depth for the contiguous US), in which PRFs provide relatively clean images. It is also in this depth range that we observe the best agreement between our S-reflection and PRF profiles. We do not entirely understand why our results do not agree better with existing SRF results, but it is possible that the more limited depth resolution of SRFs compared to topside S reflections and PRFs (given the pulse frequencies and ray geometries involved) cause SRFs to be sensitive to different vertical scales.

Ultimately, there is a need for joint inversions that include both topside reflections and converted phases to exploit all the information in the upcoming teleseismic wavefield (e.g., Bostock et al. (2001), Kumar and Bostock (2006), Monteiller et al. (2015)). Not only could this provide more robust results for imaging interfaces, but also holds the potential to discriminate between different models for the changes in material properties at the interfaces, such as velocity drops caused by partial melt or changes in anisotropy strength or orientation. By combining data from multiple phases within both the P-SV and SH systems, it should be possible to obtain a more complete understanding of lithospheric structure than is possible from analyzing a single scattered or converted phase. Joint inversions of receiver functions with surface waves (e.g., Bodin et al. (2012), Julia et al. (2000), Shen et al. (2013)) have also proven useful by combining the power of surface waves to resolve large-scale absolute seismic velocities, albeit with limited depth resolution, and the sensitivity of body-wave converted and reflected phases to sharp velocity changes.

5 Conclusions

We construct high-resolution images of lithospheric discontinuities beneath the contiguous United States using teleseismic SH reflections from deep earthquakes recorded by the Transportable Array and other regional seismic networks. In the western US, our results resolve the lithosphere-asthenosphere boundary at a depth between 60 and 110 km depth, with characteristics that correlate well with active tectonic features in the area. In the Central and Eastern US, we observe two mid-lithospheric discontinuities in the depth ranges of 60–100 km and 100–150 km, respectively, which appear associated with past tectonic events. Our results show agreement with the results of P receiver functions in many regions, which implies the possibility of jointly constraining the properties of lithospheric discontinuities with both S-reflection and P-receiver-function observations.

Acknowledgments

This study is funded by NSF Grants EAR-1358510 and EAR-1829601. T.L. is supported by a Green Postdoctoral Scholarship. The data used in this study is freely available through the Incorporated Research Institutions for Seismology Data Management Center (IRIS DMC)https://ds.iris.edu/ds/nodes/dmc/. IRIS DMC is funded by the the NSF under Cooperative Support Agreement EAR-1851048. Data from the following seismic networks is used in this study: AE-Arizona Broadband SeismicNetwork; AG-Arkansas Seismic Network; BK-Berkeley Digital Seismograph Network; CC-Cascade Chain Volcano Monitoring; CI-Caltech Regional Seismic Network; CN-Canadian National Seismograph Network; CO-South Carolina Seismic Network; IE-INL Seismic Monitoring Program; IU-Global Seismograph Network; IW-Intermountain West Seismic Network; LD-Lamont-Doherty Lamont-Doherty Cooperative Seismographic Network; N4-Central and Eastern US Net-

work; NC-USGS Northern California Regional Network; NE-New England Seismic Network; NM-Cooperative New Madrid Seismic Network; NN-Nevada Seismic Network; OH-Ohio Seismic Network; OK-Oklahoma Seismic Network; PE-Pennsylvania State Seismic Network; TA-Transportable Array; TX-Texas Seismological Network; US-United States National Seismic Network; UU-University of Utah Regional Seismic Network; UW-Pacific Northwest Seismic Network; WU-Southern Ontario Seismic Network; WY-Yellowstone National Park Seismograph Network. We thank Karen Fischer and Shun Ichiro-Karato for stimulating discussion. We thank Rainer Kind and an anonymous reviewer for their critical comments, which greatly improved our manuscript.

References

Bodin, T., Sambridge, M., Tkalčić, H., Arroucau, P., Gallagher, K., & Rawlinson, N. (2012). Transdimensional inversion of receiver functions and surface wave dispersion. *Journal of Geophysical Research: Solid Earth*, *117*(B2).

Bostock, M., Rondenay, S., & Shragge, J. (2001). Multiparameter two-dimensional inversion of scattered teleseismic body waves 1. theory for oblique incidence. *Journal of Geophysical Research: Solid Earth*, *106*(B12), 30771–30782.

Buehler, J., & Shearer, P. (2017). Uppermost mantle seismic velocity structure beneath usarray. *Journal of Geophysical Research: Solid Earth*, *122*(1), 436–448.

Crotwell, H. P., & Owens, T. J. (2005). Automated receiver function processing. *Seismological Research Letters*, *76*(6), 702–709.

Fenneman, N. M. (1946). *Physical divisions of the united states* (Tech. Rep.). US Geological Survey.

Ford, H. A., Fischer, K. M., Abt, D. L., Rychert, C. A., & Elkins-Tanton, L. T. (2010). The lithosphere–asthenosphere boundary and cratonic lithospheric layering beneath australia from sp wave imaging. *Earth and Planetary Science Letters*, *300*(3-4), 299–310.

Hammond, W. C., Blewitt, G., & Kreemer, C. (2014). Steady contemporary deformation of the central basin and range province, western united states. *Journal of Geophysical Research: Solid Earth*, *119*(6), 5235–5253.

Hansen, R. T., Bostock, M. G., & Christensen, N. I. (2012). Nature of the low velocity zone in cascadia from receiver function waveform inversion. *Earth and Planetary Science Letters*, *337*, 25–38.

Hansen, S. M., Dueker, K., & Schmandt, B. (2015). Thermal classification of lithospheric discontinuities beneath usarray. *Earth and Planetary Science Letters*, *431*, 36–47.

Hawley, W. B., Allen, R. M., & Richards, M. A. (2016). Tomography reveals buoyant asthenosphere accumulating beneath the juan de fuca plate. *Science*, *353*(6306), 1406–1408.

Hayes, G. P., Moore, G. L., Portner, D. E., Hearne, M., Flamme, H., Furtney, M., & Smoczyk, G. M. (2018). Slab2, a comprehensive subduction zone geometry model. *Science*, *362*(6410), 58–61.

Holtzman, B., Kohlstedt, D. L., Zimmerman, M. E., Heidelbach, F., Hiraga, T., & Hustoft, J. (2003). Melt segregation and strain partitioning: Implications for seismic anisotropy and mantle flow. *Science*, *301*(5637), 1227–1230.

Holtzman, B. K., & Kendall, J.-M. (2010). Organized melt, seismic anisotropy, and plate boundary lubrication. *Geochemistry, Geophysics, Geosystems*, *11*(12).

Hopper, E., & Fischer, K. M. (2018). The changing face of the lithosphere-asthenosphere boundary: Imaging continental scale patterns in upper mantle structure across the contiguous us with sp converted waves. *Geochemistry, Geophysics, Geosystems*, *19*(8), 2593–2614.

Julia, J., Ammon, C., Herrmann, R., & Correig, A. M. (2000). Joint inversion of receiver function and surface wave dispersion observations. *Geophysical Journal International*, *143*(1), 99–112.

Karato, S.-i. (2012). On the origin of the asthenosphere. *Earth and Planetary Science Letters*, *321*, 95–103.

Karato, S.-i., Olugboji, T., & Park, J. (2015). Mechanisms and geologic significance of the mid-lithosphere discontinuity in the continents. *Nature Geoscience*, *8*(7), 509–514.

Katz, R. F., Spiegelman, M., & Holtzman, B. (2006). The dynamics of melt and shear localization in partially molten aggregates. *Nature*, *442*(7103), 676–679.

Kawakatsu, H., Kumar, P., Takei, Y., Shinohara, M., Kanazawa, T., Araki, E., & Suyehiro, K. (2009). Seismic evidence for sharp lithosphere-asthenosphere boundaries of oceanic plates. *Science*, *324*(5926), 499–502.

Kennett, B., & Engdahl, E. (1991). Traveltimes for global earthquake location and phase identification. *Geophysical Journal International*, *105*(2), 429–465.

Kind, R., Mooney, W. D., & Yuan, X. (2020). New insights into the structural elements of the upper mantle beneath the contiguous united states from s-to-p converted seismic waves. *Geophysical Journal International*, *222*(1), 646–659.

Kumar, M. R., & Bostock, M. (2006). Transmission to reflection transformation of teleseismic wavefields. *Journal of Geophysical Research: Solid Earth*, *111*(B8).

Levander, A., & Miller, M. S. (2012). Evolutionary aspects of lithosphere discontinuity structure in the western us. *Geochemistry, Geophysics, Geosystems*, *13*(7).

Liu, L., & Gao, S. S. (2018). Lithospheric layering beneath the contiguous united states constrained by s-to-p receiver functions. *Earth and Planetary Science Letters*, *495*, 79–86.

Liu, T., Klemperer, S. L., Ferragut, G., & Yu, C. (2019). Post-critical sspmp and its applications to virtual deep seismic sounding (vdss)–2: 1-d imaging of the crust/mantle and joint constraints with receiver functions. *Geophysical Journal International*, *219*(2), 1334–1347.

Martinez, L. J., Meertens, C. M., & Smith, R. B. (1998). Rapid deformation rates along the wasatch fault zone, utah, from first gps measurements with implications for earthquake hazard. *Geophysical research letters*, *25*(4), 567–570.

Monteiller, V., Chevrot, S., Komatitsch, D., & Wang, Y. (2015). Three-dimensional full waveform inversion of short-period teleseismic wavefields based upon the sem–dsm hybrid method. *Geophysical Journal International*, *202*(2), 811–827.

Plank, T., & Forsyth, D. W. (2016). Thermal structure and melting conditions in the mantle beneath the basin and range province from seismology and petrology. *Geochemistry, Geophysics, Geosystems*, *17*(4), 1312–1338.

Rychert, C. A., Fischer, K. M., & Rondenay, S. (2005). A sharp lithosphere–asthenosphere boundary imaged beneath eastern north america. *Nature*, *436*(7050), 542–545.

Rychert, C. A., & Shearer, P. M. (2009). A global view of the lithosphere-asthenosphere boundary. *Science*, *324*(5926), 495–498.

Savage, B., & Silver, P. G. (2008). Evidence for a compositional boundary within the lithospheric mantle beneath the kalahari craton from s receiver functions. *Earth and Planetary Science Letters*, *272*(3-4), 600–609.

Shearer, P. M. (1991). Constraints on upper mantle discontinuities from observations of long-period reflected and converted phases. *Journal of Geophysical Research: Solid Earth*, *96*(B11), 18147–18182.

Shearer, P. M., & Buehler, J. (2019). Imaging upper-mantle structure under usarray using long-period reflection seismology. *Journal of Geophysical Research: Solid Earth*, *124*(9), 9638–9652.

Shen, W., & Ritzwoller, M. H. (2016). Crustal and uppermost mantle structure beneath the united states. *Journal of Geophysical Research: Solid Earth*, *121*(6), 4306–4342.

Shen, W., Ritzwoller, M. H., & Schulte-Pelkum, V. (2013). A 3-d model of the crust and uppermost mantle beneath the central and western us by joint inversion of receiver functions and surface wave dispersion. *Journal of Geophysical*

Research: Solid Earth, *118*(1), 262–276.

Thatcher, W., Foulger, G., Julian, B., Svarc, J., Quilty, E., & Bawden, G. (1999). Present-day deformation across the basin and range province, western united states. *Science*, *283*(5408), 1714–1718.

Yuan, H. (2015). Secular change in archaean crust formation recorded in western australia. *Nature Geoscience*, *8*(10), 808–813.

Zhu, H., Komatitsch, D., & Tromp, J. (2017). Radial anisotropy of the north american upper mantle based on adjoint tomography with usarray. *Geophysical Journal International*, *211*(1), 349–377.

Zhu, L., & Kanamori, H. (2000). Moho depth variation in southern california from teleseismic receiver functions. *Journal of Geophysical Research: Solid Earth*, *105*(B2), 2969–2980.

Journal of Geophysical Research - Solid Earth

Supporting Information for

Complicated lithospheric structure beneath the contiguous US revealed by teleseismic S reflections

Tianze Liu[1], Peter M. Shearer[1]

[1]Institute of Geophysics and Planetary Physics, Scripps Institution of Oceanography, UC San Diego

Contents of this file

Figures S1 to S5

Introduction

This supplementary information contains Supplementary Figures 1–5 and their captions.

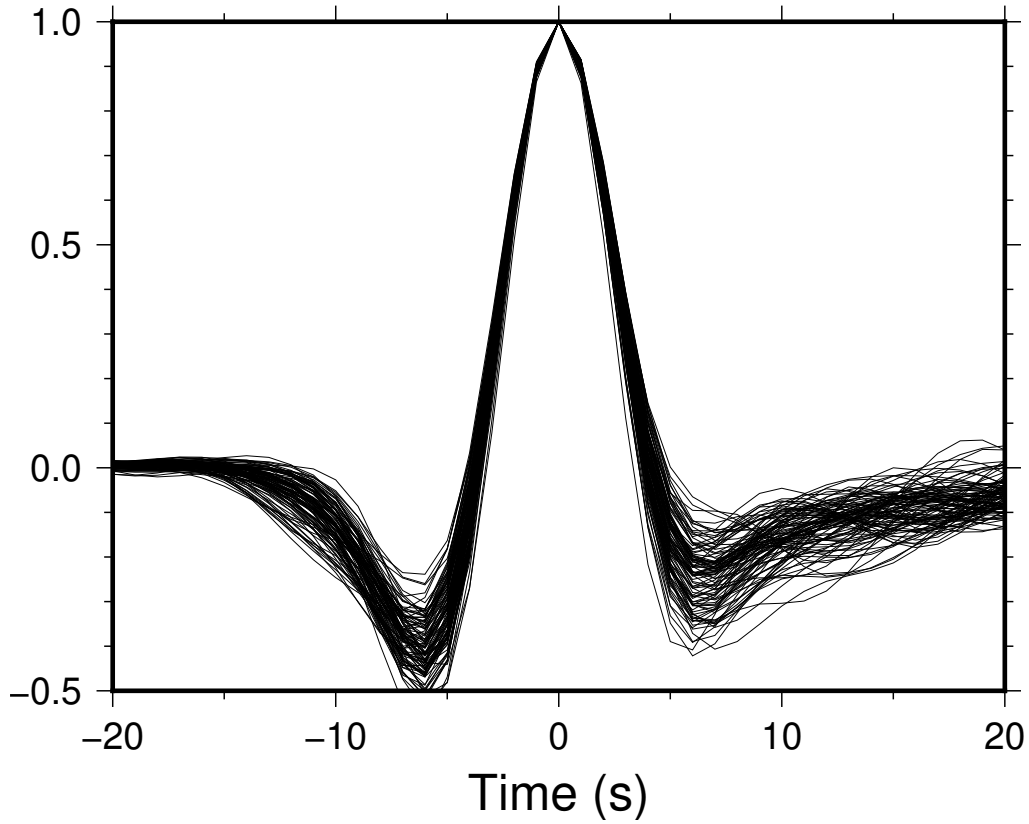

Figure S1. Stacked reference pulses of 100 randomly selected bins of our CRP image. All the stacks include more than 100 traces.

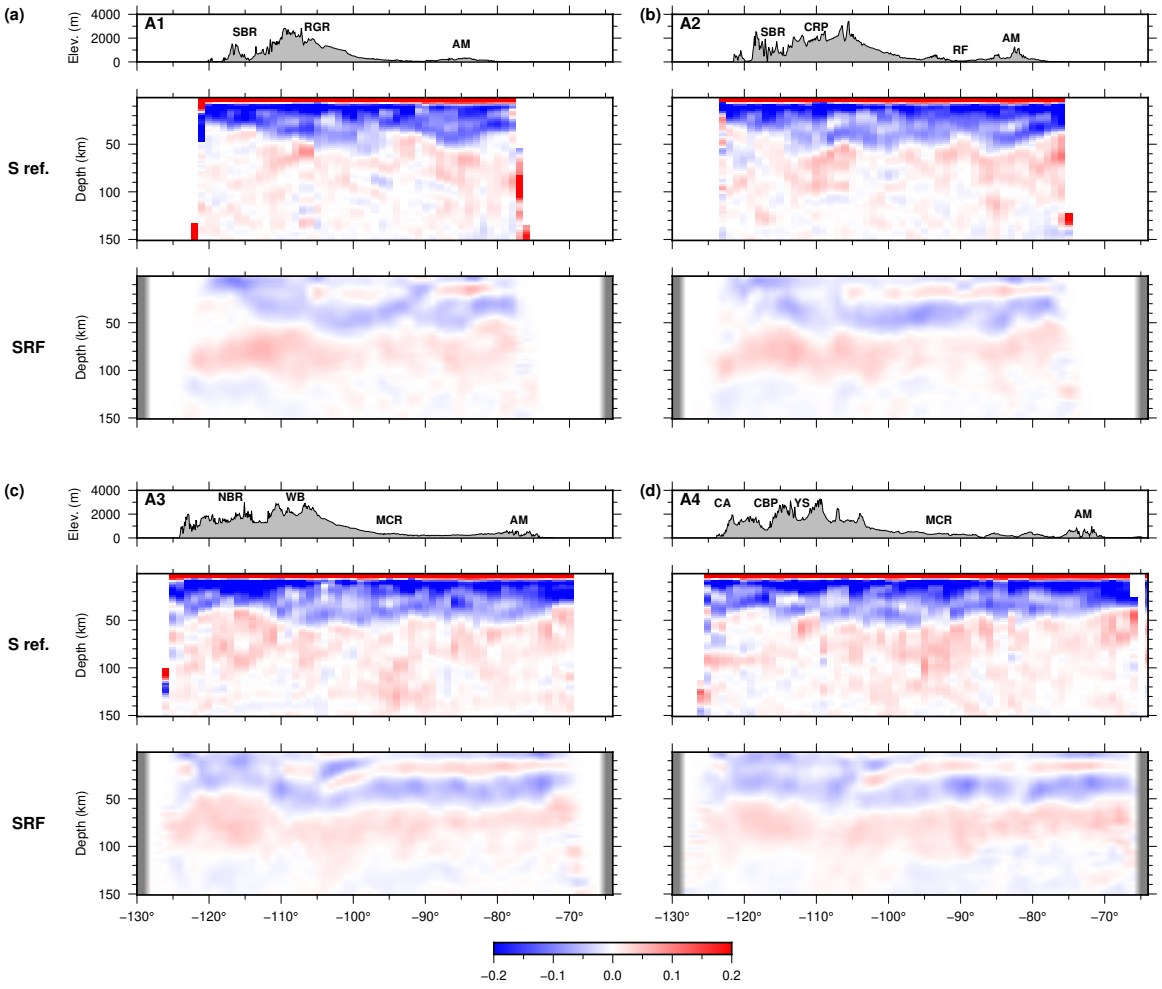

Figure S2. Comparison between our S-reflection CRP images with the SRF images from Hopper & Fischer (2018) along (a) Profile A1, (b) Profile A2, (c) Profile A3, and (d) Profile A4. See Fig. 5 for the location of the profiles and Fig. 5 for the acronyms of key tectonic features.

.

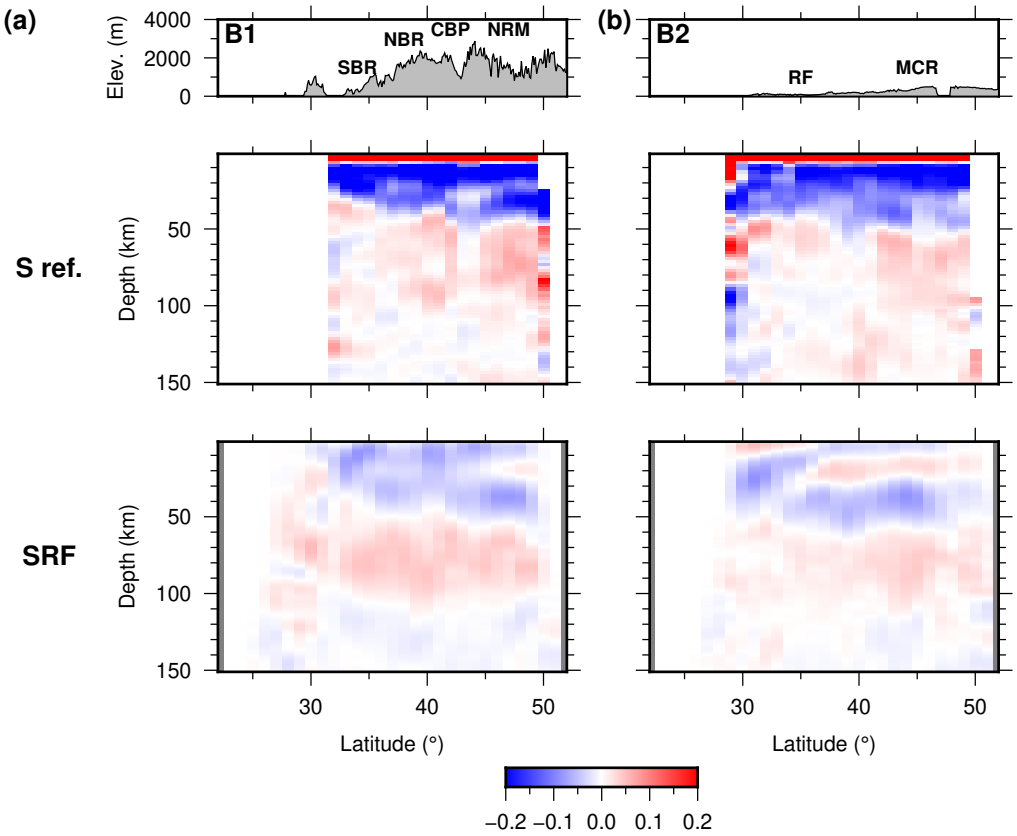

Figure S3. Comparison between our S-reflection CRP images with the SRF images from Hopper & Fischer (2018) along (a) Profile B1, (b) Profile B2. See Fig. 5 for the location of the profiles and Fig. 5 for the acronyms of key tectonic features.

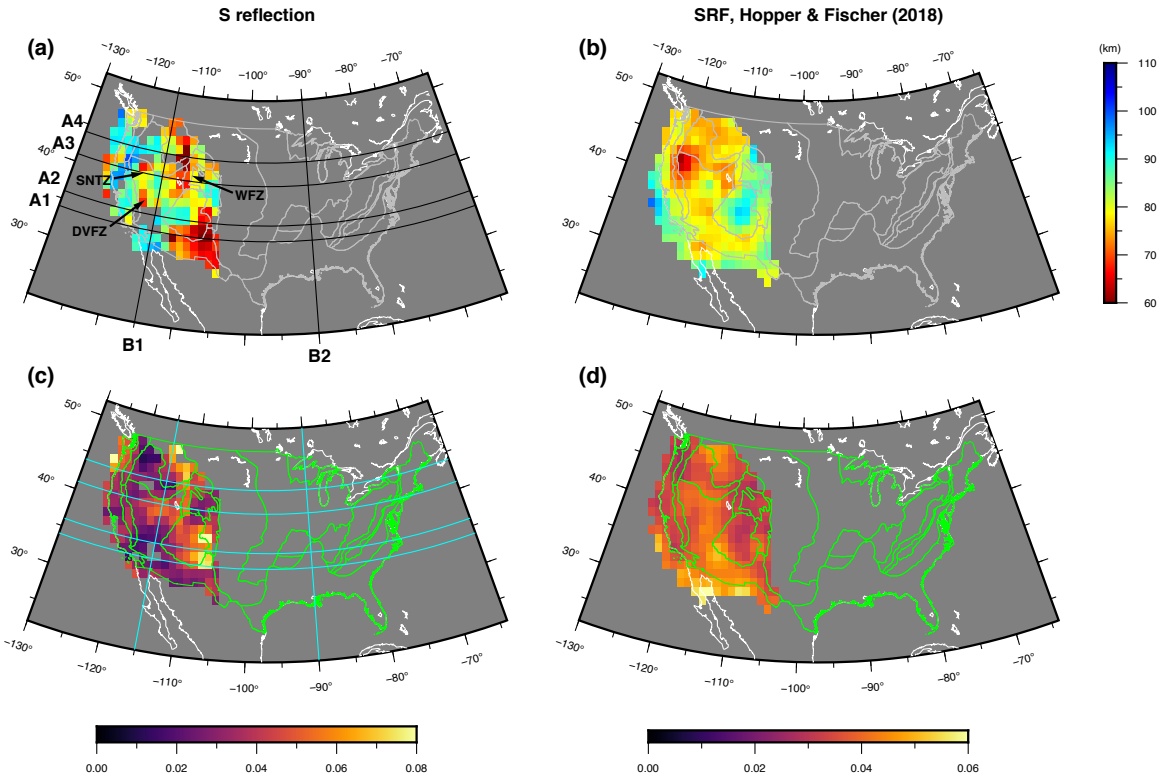

Figure S4. LAB depth and amplitude maps derived from (a) and (c) our S-reflection image and (b) and (d) the SRF image of Hopper & Fischer (2018).

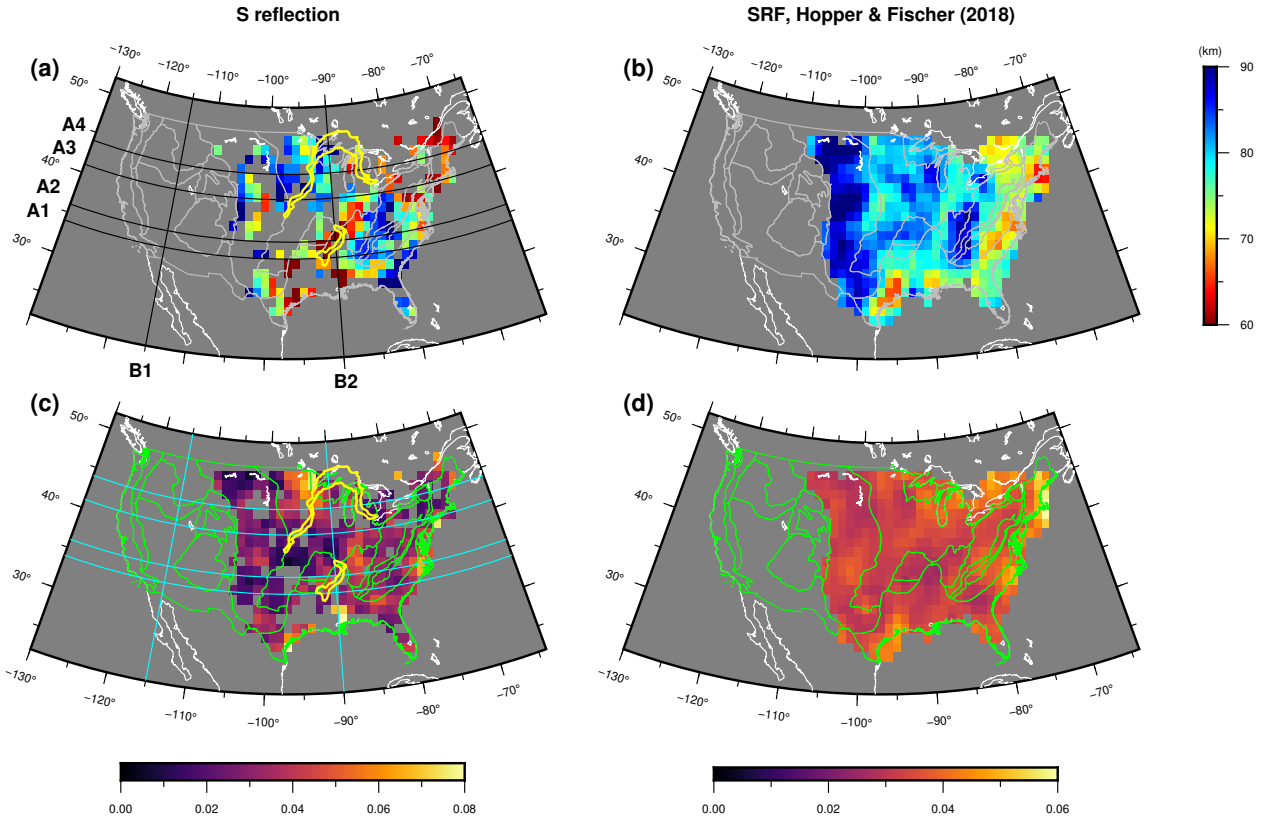

Figure S5. Depth and amplitude maps of (a) and (c) the near-Moho MLD derived from our S-reflection image and (b) and (d) the maximum negative velocity gradient derived from the SRF image of Hopper & Fischer (2018) in the CEUS.